

1 A Pooled Neuronal Activity Screen Links TMEM50A-Dependent MVB Function

2 to Synaptic Integrity and Remote Memory

4 Jianhui Wang,^{1,2†} Meiqi Liu,^{3,4†} Yiming Chen,^{1,2†} Jiancheng Chen,^{3,4} Xin Zhong,^{1,2}
5 Zilong Wang,^{1,2*} Xian Jiang,^{3,4*} Ruilin Tian^{1,2*}

6

7 ¹SUSTech Homeostatic Medicine Institute, Department of Medical Neuroscience,
8 School of Medicine, Southern University of Science and Technology, Shenzhen
9 518055, China

¹⁰Key University Laboratory of Metabolism and Health of Guangdong, Southern
¹¹University of Science and Technology, Shenzhen 518055, China

12 ³Institute of Neurological and Psychiatric Disorders, Shenzhen Bay Laboratory,
13 Shenzhen 518132, China

¹⁴ ⁴School of Chemical Biology and Biotechnology, Peking University Shenzhen
¹⁵ Graduate School, Shenzhen 518055, China

16 †These authors contributed equally

¹⁷ *Correspondence: wangzl6@sustech.edu.cn (Z.W.), jiangxian@szbl.ac.cn (X.J.) and
¹⁸ tianrl@sustech.edu.cn (R.T.)

19

20 **Abstract**

21 While advances in omics profiling have rapidly expanded the catalog of genes
22 associated with brain activity in health and disease, functional annotation has lagged
23 far behind. Here, we establish a high-throughput functional genomics platform that
24 couples the calcium-integrating sensor CaMPARI2 with CRISPRi screening in human
25 iPSC-derived neurons. By converting cumulative neuronal activity into a stable, flow
26 cytometry-readable signal, this approach enables systematic interrogation of neuronal
27 activity through pooled screening. Using a focused library of memory-associated genes,
28 we recover known regulators and identify TMEM50A, a previously uncharacterized

29 protein, as essential for neuronal activity. TMEM50A forms a complex with
30 LEPROT1 and associates with ESCRT-III machinery on multivesicular bodies
31 (MVBs). TMEM50A loss impairs MVB function, remodels the neuronal surface
32 proteome, reduces synapse density, and alters behavior in mice. This platform enables
33 systematic discovery of neuronal activity regulators and reveals a critical role for
34 TMEM50A-dependent MVB function in maintaining synaptic integrity and behavior.

35

36 **Teaser**

37 A novel CaMPARI2-based CRISPRi screening reveals TMEM50A's role in neuronal
38 activity and synaptic integrity.

39

40 INTRODUCTION

41 Neuronal activity is a unique physiological property of neurons, fundamental to their
42 function and tightly regulated to support behavior. Its dysregulation contributes to
43 diverse neurological diseases, including epilepsy¹, neurodegenerative diseases², and
44 neurodevelopmental disorders^{3,4}. Neuronal activity is shaped by the intrinsic
45 excitability of individual neurons and by their synaptic connectivity and strength within
46 neural circuits. Although many key regulators have been identified, including ion
47 channels^{5–8}, synaptic assembly factors⁹ and transcriptional and post-translational
48 modulators^{10,11}, the molecular mechanisms controlling neuronal activity remain
49 incompletely characterized and lack systematic investigation.

50

51 Rapid advances in omics profiling technologies have greatly expanded the scale of
52 candidate gene discovery linked to behavior-associated neuronal activity. For example,
53 single-cell transcriptomics have revealed hundreds to thousands of differentially
54 expressed genes (DEGs) in neurons that are active during learning and memory^{12–15}.
55 However, a major challenge is to move beyond expression correlations to pinpoint
56 genes, from these long candidate lists, that causally regulate neuronal activity and
57 behavior, and to define the molecular and cellular mechanisms through which they act.

58

59 Systematic identification of genes regulating neuronal activity has been hindered by the
60 lack of high-throughput screening tools for neuronal activity phenotypes. Patch-clamp
61 electrophysiology provides gold-standard measurements but is technically demanding
62 and low-throughput^{16,17}. Voltage and calcium imaging with chemical or genetically
63 encoded probes offer optical readout of neuronal activity but capture transient, dynamic
64 signals that require real-time monitoring with fluorescence microscopy or microplate
65 readers^{18–20}, constraining throughput to low- or medium-scale arrayed formats (Figure
66 1A).

67

68 CaMPARI (Calcium-Modulated Photoactivatable Ratiometric Integrator) offers an
69 alternative strategy for calcium-based neuronal activity detection^{21–24}. Unlike real-time

70 calcium indicators. CaMPARI is a calcium integrator, capable of recording cumulative
71 calcium activity over defined time periods. Under conditions of elevated intracellular
72 calcium, coincident illumination with violet light induces irreversible photoconversion
73 of CaMPARI from green to red fluorescence. This property enables the conversion of
74 neuronal activity—which is accompanied by Ca^{2+} influx—during a defined
75 illumination window into a stable, integrated fluorescence parameter: the red-to-green
76 (R/G) ratio. CaMPARI has thus been adopted for *in vivo* labeling of behaviorally
77 relevant neuronal ensembles^{25,26}.

78

79 Here, we leveraged CaMPARI's unique ability to convert cumulative neuronal activity
80 into a single, stable fluorescence parameter and coupled it with fluorescence-activated
81 cell sorting (FACS), establishing a high-throughput method for detecting neuronal
82 activity at single-cell resolution (Figure 1A). We further integrated this activity-based
83 sorting approach with a CRISPRi genetic screening platform in human induced
84 pluripotent stem cell (iPSC)-derived neurons (iNeurons)²⁷, developing a pooled high-
85 throughput screening method for neuronal activity. As a proof-of-principle, we applied
86 our CaMPARI-CRISPRi platform to screen a group of DEGs identified via single-cell
87 RNA sequencing (scRNA-seq) during long-term memory formation¹³. Our screen
88 uncovered both known and previously uncharacterized modulators of neuronal activity.
89 Notably, we identify *TMEM50A*, a gene of previously unknown function, as an essential
90 factor for neuronal activity that acts by controlling multivesicular body (MVB)
91 formation. Loss of *TMEM50A* reduces synapse density, disrupts neuronal
92 electrophysiological properties, and alters behavior in mice, including deficits in remote
93 memory.

94

95 **RESULTS**

96 **Establishing a CaMPARI2-based high-throughput method to quantify neuronal 97 activity in human iNeurons**

98 The Ca^{2+} -dependent, irreversible photoconversion of CaMPARI converts transient
99 neuronal activity into a stable fluorescence readout, quantified as the red-to-green (R/G)

100 ratio. This enables cumulative neuronal activity to be measured post hoc in a high-
101 throughput, scalable manner by flow cytometry: for a fixed illumination window, a
102 higher CaMPARI R/G ratio indicates greater Ca^{2+} accumulation and therefore stronger
103 neuronal activity (Figure 1A).

104

105 To enable pooled CRISPR screens of neuronal activity, we integrated CaMPARI into
106 our previously developed CRISPRi screening platform in human iNeurons. We
107 introduced CaMPARI2, an improved version of CaMPARI, via lentiviral infection into
108 iPSCs harboring doxycycline-inducible NGN2 cassette in the AAVS1 safe harbor locus
109 and CRISPRi machinery (dCas9-BFP-KRAB) cassette in the CLYBL locus²⁸ (Figure
110 1B). Upon NGN2 induction, iPSCs rapidly differentiate into glutamatergic neurons²⁹.
111 These iNeurons are functional excitatory neurons that form excitatory synapses and
112 exhibit robust spontaneous and evoked activity, with electrophysiological properties
113 reaching a steady state at 4–6 weeks³⁰.

114

115 Consistent with prior characterization, RNA-seq analysis of our iNeurons at different
116 stages of differentiation (days 14, 21, 28, and 35) revealed marked upregulation of
117 genes associated with neuronal activity—including ion channels, glutamate receptors,
118 vesicle release machinery, and synapse formation—after day 14, plateauing at days 21–
119 28 (Figure 1C). Whole-cell patch-clamp recordings of spontaneous and current
120 injection-evoked action potential firing further confirmed that day-28 iNeurons exhibit
121 robust neuronal activity (Figure 1D). We therefore used day-28 iNeurons in subsequent
122 experiments.

123

124 We next characterized whether CaMPARI2 can reliably detect neuronal activity in
125 iNeurons. Using fluorescence microscopy, we observed robust photoconversion in
126 CaMPARI2-iNeurons illuminated with violet light for 5 min (Figure 1E). Importantly,
127 this photoconversion was readily quantified by flow cytometry, with the R/G intensity
128 ratio increasing as a function of illumination time over the 0–10 min range. To ensure

129 sufficient signal while minimizing light-induced cytotoxicity, we used 5 min of
130 illumination in subsequent experiments.

131

132 We then tested whether CaMPARI2 captures neuronal activity changes. Glutamate
133 stimulation of iNeurons elicited a dose-dependent increase in CaMPARI2
134 photoconversion, demonstrating that CaMPARI2 reliably reports neuronal activity in
135 response to excitatory input (Figure 1G). To determine whether CaMPARI2 can also
136 detect genetically driven activity modulation, we performed CRISPRi knockdown of
137 two established regulators of neuronal excitability and synaptic function: *TSC1*³¹, a key
138 negative regulator of mTOR signaling implicated in epilepsy and neurodevelopmental
139 disorders, and *STXBP1*²⁹, which encodes a presynaptic vesicle release factor and is
140 associated with developmental and epileptic encephalopathy³². Consistent with reports
141 of decreased activity associated with loss of these genes, flow cytometry revealed
142 reduced CaMPARI2 R/G ratios under both 1-min and 5-min illumination following
143 knockdown of either *TSC1* or *STXBP1* in iNeurons (Figure 1H). Collectively, these data
144 establish CaMPARI2 photoconversion as a robust, scalable, flow cytometry-
145 compatible readout for quantifying neuronal activity in human iNeurons.

146

147 **A CaMPARI2-based CRISPRi screen uncovers known and novel neuronal 148 activity regulators**

149 Next, we conducted a proof-of-principle CaMPARI2-based neuronal activity screen in
150 iNeurons. To maximize the chance of identifying key regulators, we constructed a
151 biologically informed sgRNA library targeting a set of high-confidence remote-
152 memory-associated DEGs in excitatory neurons identified in a recent scRNA-seq
153 study¹³. These memory-associated genes reflect stable, long-lasting transcriptional
154 programs linked to remote memory storage and are enriched for pathways involved in
155 synaptic function, neuronal excitability, and activity-dependent plasticity. The sgRNA
156 library comprised 320 sgRNAs targeting 64 genes (5 sgRNAs per gene), alongside 28
157 non-targeting control sgRNAs (Figure 2A, Table S1). The library was delivered into
158 CaMPARI2-expressing CRISPRi-iPSCs via lentiviral infection, followed by selection,

159 expansion, and differentiation. At Day 28, neurons were illuminated with violet light
160 for 5 min to induce activity dependent CaMPARI2 photoconversion. Subsequently,
161 neurons were sorted by FACS into populations with the highest 30% or lowest 30%
162 R/G ratios. Next-generation sequencing (NGS) was then used to quantify sgRNA
163 representation in each population, and hits were called using the MAGeCK-iNC
164 pipeline^{27,33}.

165

166 The screen uncovered both positive and negative hits, whose knockdown increased or
167 decreased CaMPARI2 signal respectively (Figure 2B, Table S2). Among the hits, we
168 recovered multiple genes previously implicated in synaptic function, intrinsic
169 excitability, or epilepsy³⁴, including *ATP6V0C*³⁵, *HNRNPH2*³⁶, *NSF*³⁷, *STX1B*³⁸,
170 *NCDN*³⁹, *GSK3B*⁴⁰, *PAK1*⁴¹, *SDHA*⁴², *VAMP2*⁴³, *PIGQ*⁴⁴, and *ALG2*³⁴, validating
171 the reliability of our screening strategy.

172

173 Interestingly, among the negative hits we identified *TMEM50A*, a putative
174 transmembrane protein with previously uncharacterized function (Figure 2B), and
175 therefore prioritized it for follow-up. To confirm the *TMEM50A* phenotype and rule out
176 potential sgRNA off-target effects, we individually cloned three independent sgRNAs
177 targeting *TMEM50A*. Knockdown of *TMEM50A* with each of the three sgRNAs in
178 iNeurons significantly reduced CaMPARI2 photoconversion compared to non-
179 targeting controls (Figure 2C, S2A), thereby validating the screening result, and
180 excluding off-target effects.

181

182 To determine whether the reduction in CaMPARI2 signal reflected bona fide changes
183 in neuronal activity, we generated *TMEM50A* knockout (KO) iPSCs (Figure S2B–C)
184 and assessed the electrophysiological properties of the derived iNeurons using whole-
185 cell patch-clamp. Voltage-clamp recordings revealed a significant reduction in both
186 sEPSC frequency and amplitude in *TMEM50A* KO iNeurons, indicating a marked
187 impairment in synaptic transmission (Figure 2D–E). Additionally, current-clamp
188 analysis showed that *TMEM50A* KO iNeurons exhibited a significant reduction in the

189 number of action potentials generated in response to depolarizing current steps
190 compared to controls (Figure 2F-G), indicating reduced intrinsic excitability. Together,
191 these data demonstrate that TMEM50A is critical for maintaining neuronal activity
192 levels by supporting both excitatory synaptic drive and intrinsic neuronal
193 responsiveness.

194

195 In summary, our CaMPARI2-based CRISPRi screen provides a robust approach for
196 identifying neuronal activity regulators and identifies TMEM50A as a novel factor
197 required to maintain normal neuronal activity in human iNeurons.

198

199 **TMEM50A localizes to multivesicular bodies**

200 TMEM50A is predicted to encode a four-pass transmembrane protein (Figure S1A) and
201 is highly conserved across vertebrates (Figure S1B). *TMEM50A* has a paralog in the
202 human genome, TMEM50B; however, *TMEM50A* is the predominant paralog
203 expressed in iNeurons, with consistently higher expression than *TMEM50B* across
204 differentiation stages (Figure S1C).

205

206 To begin elucidating how TMEM50A regulates neuronal activity, we first determined
207 its subcellular localization. Because of the lack of suitable antibodies, we initially
208 examined its localization using a fluorescently tagged TMEM50A construct
209 (TMEM50A–HA–GFP) in COS7 cells. However, we found that the expression level of
210 exogenous TMEM50A profoundly affect its localization: transient overexpression
211 produced prominent co-localization with the ER marker Sec61B⁴⁵, whereas lower-level
212 expression via lentiviral transduction reduced the reticular ER signal and revealed a
213 punctate, vesicle-like distribution (Figure S3A). Live-cell imaging further showed that
214 these vesicles were motile and moved along the ER network (Movie S1).

215

216 To determine the localization of endogenous TMEM50A, we generated C-terminal
217 3×FLAG–mNeonGreen knock-in (KI) lines using CRISPR/Cas9-mediated homology-

218 directed repair (HDR) in both HEK293T cells and iPSCs (Figure S3B). Using super-
219 resolution structured illumination microscopy (SIM), we observed predominantly
220 vesicular localization of TMEM50A in both HEK293T KI cells and iNeurons derived
221 from the iPSC KI line. In iNeurons, TMEM50A-positive vesicles were detected in both
222 soma and neurites (Figure 3B–C; Movies S2–S4).

223

224 To define the identity of these vesicles, we performed co-localization analysis with
225 markers of distinct membrane compartments⁴⁶, including mRuby-RAB1A (ERGIC),
226 mRuby-RAB5A (early endosome), mRuby-RAB7A (late endosome),
227 mRuby-RAB11A (recycling endosome), and LAMP1 (lysosome). TMEM50A showed
228 predominant co-localization with endosomal markers but not lysosomes (Figure S3C–
229 D).

230

231 We next performed interactome profiling by immunoprecipitation–mass spectrometry
232 (IP–MS) using FLAG pull-down from TMEM50A–3×FLAG–mNeonGreen knock-in
233 iNeurons, with IgG pull-down as a control (Figure 3D; Table S3). Notably, many
234 TMEM50A interactors are involved in vesicular trafficking, including AP2B1⁴⁷,
235 AP2M1⁴⁸, AP2S1⁴⁹, AP2A2⁴⁷, RAB11B^{46,50}, TMEM87A⁵¹, PIK3R4⁵², and
236 VPS51⁵³. In addition, several ESCRT/MVB-related factors were identified, including
237 CHMP7⁵⁴, CHMP1B⁵⁴, CHMP4B⁵⁴, VTA1⁵⁵, and HGS⁵⁶. Gene Ontology analysis
238 further highlighted enrichment for MVB-related pathways (Figure 3E). Consistent with
239 these proteomic data, co-localization analysis with the MVB marker CD63 confirmed
240 that TMEM50A is enriched on MVBs (Figure 3F).

241

242 **TMEM50A forms a complex with LEPROTL1 and interacts with ESCRT-III to
243 maintain MVB function**

244 Among the TMEM50A interactors identified by IP–MS, LEPROTL1 emerged as a
245 particularly interesting candidate. Although LEPROTL1 function in mammalian cells
246 remains poorly characterized, its yeast homolog Vps55 has been reported to interact
247 with Vps68, the yeast homolog of TMEM50A^{57,58}. AlphaFold3-based structural

248 modeling revealed that yeast Vps55, Vps68, and the Vps55–Vps68 complex closely
249 resemble human LEPROT1, TMEM50A, and the LEPROT1–TMEM50A complex,
250 respectively, with RMSD values of 1.03 Å, 3.44 Å, and 1.25 Å (Figure 4A).

251

252 To determine whether TMEM50A forms a similar complex with LEPROT1 in
253 mammalian cells, we performed co-immunoprecipitation (co-IP) experiments, which
254 demonstrated a robust association between TMEM50A and LEPROT1 (Figure 4B).
255 Consistently, immunofluorescence analysis revealed strong co-localization of
256 TMEM50A and LEPROT1 (Figure 4C–D). Functionally, LEPROT1 knockdown
257 reduced neuronal activity to a similar extent as TMEM50A knockdown as measured by
258 CaMPARI2, and simultaneous knockdown of both genes did not further enhance the
259 phenotype relative to either single knockdown (Figure 4E; Figure 2C), indicating that
260 TMEM50A and LEPROT1 act in the same pathway as a functional complex.

261

262 Multiple ESCRT-III components, including CHMP1B, CHMP4B, and CHMP7, were
263 also identified as TMEM50A interactors (Figure 3B). Co-IP assays further confirmed
264 interactions among TMEM50A, LEPROT1, and CHMP4B (Figure 4F–G). Given the
265 central role of ESCRT-III in MVB biogenesis, we asked whether the TMEM50A–
266 LEPROT1 complex localizes with ESCRT-III on MVBs. Using TMEM50A–
267 mNeonGreen and LEPROT1–mRuby double knock-in cells, we observed substantial
268 co-localization of TMEM50A and LEPROT1 with CHMP4B and the MVB marker
269 CD63 (Figure 4H).

270

271 Based on these observations, we hypothesized that the TMEM50A–LEPROT1
272 complex supports MVB function via ESCRT-III. To test this, we performed an EGFR
273 degradation assay, in which ligand-stimulated EGFR is sorted into MVB intraluminal
274 vesicles and subsequently delivered to lysosomes for degradation⁵⁹ (Figure 4I). Notably,
275 *TMEM50A* knockout significantly delayed EGFR degradation compared to control
276 cells (Figure 4J–K), indicating defective MVB-mediated cargo degradation.

277

278 To assess the specificity of this defect, we examined lysosomal integrity using
279 LysoTracker and retrograde transport using cholera toxin B (CTxB) internalization.
280 Neither assay revealed detectable differences between *TMEM50A* knockdown and
281 control cells (Figure S4A–D).

282

283 ESCRT complexes drive intraluminal vesicle formation during MVB biogenesis
284 through membrane remodeling and scission^{60–62}. To determine the impact of
285 *TMEM50A* on MVB ultrastructure *in vivo*, we performed scanning electron
286 microscopy (SEM) on anterior cingulate cortex (ACC) sections from *Tmem50a*-KO
287 mice. Ultrastructural analysis revealed a marked reduction in the number of ILVs within
288 MVBs in *Tmem50a*-KO mice compared with WT controls (Figure 4L–M). This
289 phenotype is consistent with defects observed upon ESCRT loss⁶³, further supporting
290 a role for *TMEM50A* in ESCRT-dependent intraluminal vesicle formation during MVB
291 biogenesis.

292

293 In summary, *TMEM50A* forms a complex with LEPROT1 that associates with
294 ESCRT-III at MVBs and is required for efficient ESCRT-dependent intraluminal
295 vesicle formation and MVB-mediated cargo degradation.

296

297 ***TMEM50A* loss remodels neuron surface proteome and reduces synapse density**

298 Because MVBs play a central role in plasma membrane protein turnover^{64,65}, we
299 performed cell-surface biotinylation and affinity purification in WT and *TMEM50A* KO
300 iNeurons, followed by quantitative proteomics to measure changes in surface protein
301 abundance (Figure 5A). *TMEM50A* KO neurons showed widespread alterations in the
302 abundance of plasma membrane proteins (Figure 5B, Table S4). Gene ontology
303 analysis of the altered surface proteome revealed enrichment for pathways related to
304 cell–cell adhesion, axon guidance, and synapse organization (Figure 5C). Given the
305 synaptic transmission defects observed in *TMEM50A* KO iNeurons (Figure 2), we next
306 asked whether synapse organization is impaired. Immunostaining for the presynaptic
307 marker Synapsin1/2, the postsynaptic marker PSD95 and the dendrite marker MAP2

308 revealed a significant reduction in synaptic density in *TMEM50A* KO iNeurons. In
309 contrast, puncta size, dendrite number, and soma size showed no significant changes
310 (Figure 5D–E, S5A).

311

312 We also used mouse primary neurons to validate these findings. We isolated primary
313 cortical neurons from CRISPRi transgenic mice expressing the dCas9–KRAB
314 machinery and infected them with either a control sgRNA or a *Tmem50a*-targeting
315 sgRNA via AAV (Figure 6A). RT–qPCR confirmed a strong reduction of *Tmem50a*
316 mRNA in neurons transduced with the *Tmem50a* sgRNA (Figure 6B).
317 Immunofluorescence analysis revealed synaptic phenotypes consistent with those
318 observed in human iNeurons, showing a significant reduction in synaptic density, while
319 puncta size, dendrite number, and soma size remained unchanged (Figure 6C–D, S5B).

320

321 To assess synaptic alterations *in vivo*, we analyzed synaptic ultrastructure from the SEM
322 images of ACC sections from *Tmem50a*-KO mice. We quantified synaptic cleft width,
323 the number of synaptic vesicles (SVs) per bouton, and postsynaptic density (PSD)
324 length at both inhibitory and excitatory synapses. None of these ultrastructural
325 parameters differed significantly between *Tmem50a*-KO and WT mice (Figure 6E–F).
326 In contrast, synapse density was significantly reduced in *Tmem50a* -KO mice (Figure
327 6E–F), consistent with the reduced synaptic puncta observed in cultured neurons.

328

329 In summary, TMEM50A loss causes broad remodeling of the neuronal surface
330 proteome and leads to a reduction in synapse density.

331

332 ***Tmem50a* loss alters memory- and anxiety-related behaviors in mice**

333 Given that *TMEM50A* loss impairs neuronal activity, we asked whether it also affects
334 behavior in mice. We first assessed contextual fear memory using a standard fear-
335 conditioning paradigm (Figure 7A). *Tmem50a*-KO mice exhibited freezing behavior
336 comparable to WT controls during recent memory retrieval (Day 5), indicating intact
337 recent memory (Figure 7B). In contrast, during remote memory retrieval (Day 21),

338 *Tmem50a*-KO mice displayed significantly reduced freezing compared with WT mice,
339 indicative of impaired remote memory consolidation (Figure 7B).

340

341 We next performed the open field test (Figure 7C). *Tmem50a*-KO mice spent
342 significantly more time in the center of the arena than WT mice, suggesting reduced
343 anxiety-like behavior. Total distance traveled did not differ between *Tmem50a*-KO and
344 WT mice, indicating that this effect was not attributable to altered general locomotor
345 activity.

346

347 Finally, we assessed motor coordination using the rotarod test (Figure 7D). *Tmem50a*-
348 KO and WT mice showed no differences in latency to fall or speed at the time of fall,
349 indicating that *Tmem50a* loss does not impair motor coordination or balance.

350

351 **DISCUSSION**

352 Transcriptomic and genomic studies have generated extensive catalogs of genes
353 associated with brain activity and behavior in health and disease^{10,17,66}. Yet functional
354 characterization of these candidates has lagged far behind discovery. Here, we begin to
355 address this gap by developing a high-throughput functional genomics platform that
356 couples the calcium-integrating sensor CaMPARI2 with pooled CRISPRi screening in
357 human iPSC-derived neurons. By converting cumulative neuronal activity into a stable,
358 flow cytometry–readable signal, this system enables fluorescence-based sorting of large
359 neuronal populations by activity state, thereby supporting unbiased pooled genetic
360 screens to identify regulators of neuronal activity at scale.

361

362 Compared with patch-clamp electrophysiology and voltage or calcium imaging for
363 detecting neuronal activity, CaMPARI offers a distinct advantage as a calcium recorder:
364 activity is integrated over time and captured as a stable signal that can be measured
365 after stimulation without continuous imaging. While CaMPARI was originally
366 developed to label active neuronal ensembles *in vivo*, we demonstrate that it can
367 quantitatively detect changes in neuronal activity induced by chemical stimulation or

368 genetic perturbations when coupled with flow cytometry.

369

370 CRISPR-based functional genomics has emerged as a powerful approach for
371 systematically interrogating gene function and has been established in neuronal models.
372 Most existing screens in neurons have focused on relatively simple phenotypes, such
373 as cell survival. In this study, we extend CRISPR screening to a complex, neuron-
374 specific phenotype—neuronal activity—thereby broadening the scope of CRISPR-
375 based functional genomics in neuronal systems.

376

377 As a proof of principle, we screened a focused library of memory-associated DEGs.
378 The screen recovered established regulators of synaptic function and excitability—
379 including *NCDN*³⁹, *STX1B*⁶⁷, and *GSK3B*⁴⁰. The screen also uncovered previously
380 uncharacterized candidates, among which we selected *TMEM50A* for further validation
381 and characterization. *TMEM50A* encodes a predicted four-pass transmembrane protein
382 of unknown function in mammalian cells. Its yeast ortholog, Vps68, interacts with
383 Vps55 (the yeast homolog of LEPROT1) and with ESCRT-III components, and has
384 been implicated in vacuolar protein sorting^{57,68}. Our data indicate that these interactions
385 are conserved in mammalian cells: using IP-MS, co-immunoprecipitation, and super-
386 resolution imaging, we demonstrate that TMEM50A forms a complex with LEPROT1
387 that localizes to MVBs and associates with the ESCRT-III component CHMP4B.
388 Functionally, TMEM50A is required for efficient intraluminal vesicle formation and
389 MVB-mediated cargo degradation.

390

391 The ESCRT/MVB pathway is central to plasma membrane protein turnover and has
392 been increasingly implicated in neurological disease, including neurodegeneration and
393 synaptopathies^{69–71}. Consistent with these roles, we show that TMEM50A loss broadly
394 remodels the neuronal surface proteome, reduces synapse density, diminishes synaptic
395 transmission and intrinsic excitability, and leads to behavioral phenotypes including
396 impaired remote memory and altered anxiety-like behavior.

397

398 **Limitations and future directions**

399 First, our proof-of-principle screen used a small, focused library. Given the scalability
400 of our platform, it can be readily extended to larger, even genome-wide, libraries in
401 future studies to achieve a more systematic and comprehensive identification of genes
402 regulating neuronal activity. Additionally, this platform can be adapted to interrogate
403 neuronal activity across diverse contexts. Indeed, while this manuscript was in
404 preparation, a study utilizing a conceptually similar strategy reported screens for
405 regulators of neuronal excitability under glutamate-evoked conditions, highlighting the
406 broad applicability of pooled activity screening⁷².

407

408 Second, our screen was performed in NGN2-induced human iNeurons in 2D culture.
409 Although human iNeurons provide a tractable and reproducible system, they do not
410 fully recapitulate the complexity of the brain environment. Extending this system to
411 more complex models—such as brain organoids, assembloids, or *in vivo* settings—will
412 enable screening in more physiologically relevant contexts. Furthermore, applying this
413 platform to disease contexts, such as patient-derived iNeurons, could enable
414 identification of genetic modifiers that rescue pathological neuronal activity, leading to
415 the discovery of potential therapeutic targets.

416

417 Third, while we demonstrate that TMEM50A interacts with LEPROT1 and CHMP4B
418 to regulate MVB function, the precise molecular mechanism remains to be defined.
419 Future structural analysis and biochemical reconstitution studies will be required to
420 elucidate how the TMEM50A–LEPROT1 complex physically engages ESCRT-III
421 machinery to facilitate membrane remodeling and intraluminal vesicle biogenesis.

422

423 **MATERIALS AND METHODS**

424 **Cell Culture**

425 ***Cell lines***

426 HEK293T and COS-7 cells (ATCC) were cultured in DMEM (Gibco, C11995500BT)
427 supplemented with 10% FBS (TransGen Biotech, FS301-02) and 1% penicillin–
428 streptomycin (Aladdin, P301861) at 37 °C in a humidified incubator with 5% CO₂.
429 Cells were passaged every 2–3 d at a 1:4–1:8 split ratio using 0.05% trypsin–EDTA
430 (Yeasen, 40127ES60).

431

432 ***hiPSC culture and iNeuron differentiation***

433 hiPSCs harboring dCas9-BFP-KRAB and tet-on NGN2 (WTc11 background; Coriell
434 GM29371) were maintained in StemFlex medium (Thermo Fisher Scientific,
435 A3349401) on growth factor–reduced, phenol red–free, LDEV-free Matrigel (Corning,
436 356231) diluted 1:200 in DPBS (Invitrogen, C14190500BT). Cultures were maintained
437 at 37 °C with 5% CO₂ and fed the day after seeding and every other day thereafter. For
438 passaging at ~80% confluence, cells were rinsed with DPBS, incubated with Accutase
439 (STEMCELL Technologies, 07922) for 3–5 min at 37 °C, diluted 3–5× with DPBS,
440 gently triturated to single cells, and centrifuged at 200 × g for 5 min at room temperature.
441 Pellets were resuspended in StemFlex supplemented with Y-27632 ROCK inhibitor
442 (Selleck, S1049), counted, and replated onto fresh Matrigel-coated dishes at a 1:6–1:10
443 split ratio. ROCK inhibitor was maintained for the first 24 h post-passaging and then
444 removed.

445

446 iNeurons were generated as previously described²⁷. Briefly, hiPSCs were pre-
447 differentiated on Matrigel-coated plates in N2 pre-differentiation medium consisting of
448 KnockOut DMEM/F12, 1× MEM non-essential amino acids, 1× N2 Supplement
449 (Gibco, 17502-048), NT-3 (10 ng/mL; PeproTech, 450-03), BDNF (10 ng/mL;
450 PeproTech, 450-02), mouse laminin (1 µg/mL; Thermo Fisher Scientific, 23017-015),
451 ROCK inhibitor (10 nM), and doxycycline (2 µg/mL) to induce mNGN2 expression.
452 After 3 d, cells were replated (designated Day 0) onto plates coated with 0.1% PEI and

453 laminin in neuronal medium containing a 1:1 mixture of DMEM/F12 (Gibco, 11320-
454 033) and Neurobasal-A (Gibco, 10888-022), 1× MEM non-essential amino acids, 0.5×
455 GlutaMAX (Gibco, 35050-061), 0.5× N2 Supplement, 0.5× B27 Supplement (Gibco,
456 17504-044), NT-3 (10 ng/mL), and BDNF (10 ng/mL). Half medium was replaced
457 weekly.

458

459 ***Primary mouse neuron culture***

460 Primary cortical neurons were prepared from embryonic mice (E14–E18) as previously
461 described with minor modifications⁷³. Cortices were dissociated with 0.25% trypsin–
462 EDTA (Gibco, 25200072) for 10 min at 37 °C, followed by trituration using a Pasteur
463 pipette. Digestion was terminated with DMEM/F12 (Gibco, C11330500BT)
464 supplemented with 10% FBS (Gibco, A5669701), and DNase I was added to reduce
465 aggregation. Dissociated neurons were plated onto poly-D-lysine–coated glass
466 coverslips (Beyotime, ST508) in 24-well plates and maintained in Neurobasal medium
467 (Thermo Fisher Scientific, 10888022) supplemented with 2% B27 (Gibco, 17504044)
468 and 0.5% GlutaMAX (Gibco, 35050061) at 37 °C with 5% CO₂.

469

470 ***Mycoplasma testing***

471 Mycoplasma contamination was routinely screened by PCR, and all cultures were
472 confirmed mycoplasma-free.

473

474 **Mice**

475 *Tmem50a*-KO mice (C57BL/6JCya-Tmem50aem1) were purchased from Cyagen. This
476 line carries a conventional *Tmem50a* knockout allele generated by CRISPR/Cas9-
477 mediated deletion (NCBI Gene ID: 71817). Two guide RNAs targeting exon regions
478 were used: CTTAAGAACATATGTCAGA and AAAATTCCCAGCCCTTGGGT.
479 CRISPRi mice (H11^{dCas9-KRAB}) were purchased from The Jackson Laboratory
480 (#030000). These mice express a catalytically inactive Cas9 fused to the KRAB
481 repressor, inserted into the H11 locus of the mouse genome by targeted knock-in.
482 C57BL/6 wild-type mice were obtained from Guangdong Medical Laboratory Animal

483 Center. All mice were group-housed (maximum 5 per cage) in a specific-pathogen-free
484 (SPF) environment. They were maintained on a 12 h light–dark cycle (lights on 08:00–
485 20:00) with ad libitum access to food and water. Male mice aged 6–8 weeks were used
486 for all experiments. All surgical procedures were performed under isoflurane or
487 tribromoethanol anesthesia, and every effort was made to minimize pain and distress.
488 All animal experimental procedures were approved by the Animal Care and Use
489 Committee at Shenzhen Bay Laboratory (AEJX20220201A) and Shenzhen Medical
490 Academy of Research and Translation (SMART-IACUC-2025-A023) and conducted
491 in accordance with institutional guidelines.

492

493 **Lentiviral production**

494 HEK293T cells were seeded the day prior at ~30% density and allowed to reach ~70–
495 80% confluence on the day of transfection. For small-scale lentiviral packaging in 6-
496 well plates, 1 µg transfer plasmid and 1 µg third-generation packaging mix were diluted
497 in 200 µL Opti-MEM and combined with 6 µg PEI (Yeasen, 40816ES01) for each well.
498 For large-scale packaging of sgRNA library, one 15-cm dish was used with 15 µg
499 packaging plasmid and 15 µg library plasmid diluted in 2 mL Opti-MEM with 90 µg
500 PEI. The transfection mixture was incubated at room temperature for 15 min and then
501 added to the cells. At 48 h post-transfection, supernatants were collected, passed
502 through a 0.45 µm PVDF syringe filter into conical tubes, mixed with ¼ volume
503 lentiviral pellet solution, and held at 4 °C for 24 h. Virus-containing supernatants were
504 centrifuged at 3,500 × g for 30 min at 4 °C, the supernatant was aspirated, and a brief
505 clarification spin (3,500 × g, 2 min, 4 °C) was performed. Pellets were resuspended in
506 DPBS, aliquoted, and stored at –80 °C.

507

508 **AAV production and transduction of primary neuron**

509 Recombinant adeno-associated viruses (AAVs) were packaged at a titer of 1×10^{12} by
510 Institute of Molecular Physiology, Shenzhen Bay Laboratory. Primary cortical neurons
511 were transduced at day in vitro 4 (DIV4), with control and experimental viruses applied
512 at comparable titers.

513

514 **CaMPARI2 photoconversion assay**

515 The CaMPARI2 cassette (Addgene #101060) was subcloned into a lentiviral vector
516 containing a CAG promoter and an upstream UCOE element via Gibson assembly. A
517 stable CaMPARI2 hiPSC line was generated by lentiviral transduction of hiPSCs
518 harboring dCas9-BFP-KRAB and tet-on NGN2.

519

520 Photoconversion was induced by 405-nm LED illumination of Day 28 CaMPARI2
521 iNeurons and quantified by confocal microscopy (Nikon ECLIPSE Ts2) or flow
522 cytometry (BD FACSaria SORP). For flow cytometry, cells were enzymatically
523 dissociated with papain (Worthington, PAP2; 20 U/mL in 1× DPBS) supplemented
524 with DNase I (10 U/mL) for 15 min at 37 °C. Digestion was quenched with 3 volumes
525 of DMEM containing 10% FBS, and cells were pelleted (500 × g, 10 min). Pellets were
526 resuspended in DPBS with 5% FBS and analyzed by flow cytometry; data were
527 processed using FlowJo v10.

528

529 **Generation of sgRNA library targeting memory-associated genes**

530 A set of memory-associated genes was derived from a published scRNA-seq study that
531 identified 64 remote-memory-associated DEGs in excitatory neurons¹³. For each gene,
532 the top five sgRNAs were selected from the CRISPRi-v2 library (ref), and 28 non-
533 targeting control sgRNAs were included, yielding a final library of 348 sgRNAs (Table
534 S1). An sgRNA oligonucleotide pool was synthesized (GENEWIZ) and cloned into
535 pCRISPRia-v2 (Addgene #84832) using the BstXI and BpuI restriction sites. To assess
536 library quality, the sgRNA-containing region was PCR-amplified using Phanta Flash
537 Master Mix (Vazyme, P520) according to the manufacturer's instructions, and PCR
538 products were analyzed by next-generation sequencing.

539

540 **CaMPARI2-based CRISPRi screening**

541 sgRNA library was transduced into hiPSCs via lentiviral infection at a multiplicity of
542 infection (MOI) of ~0.3, followed by puromycin selection. After expansion, hiPSCs

543 were differentiated into iNeurons and plated at 1×10^7 cells per plate onto 10-cm PEI-
544 coated dishes.

545

546 On Day 28, iNeurons were subjected to CaMPARI2 photoconversion followed by
547 papain dissociation. Dissociated neurons were transferred to 15-mL conical tubes and
548 centrifuged at $500 \times g$ for 5 min. Pellets were gently resuspended in 2 mL DPBS, passed
549 through a 100- μ m cell strainer to remove axonal debris and incompletely dissociated
550 aggregates, and the filtrate was transferred to flow cytometry tubes for FACS.

551

552 For FACS, cells were first gated by forward and side scatter to select live singlets, then
553 sorted based on the CaMPARI2 red-to-green fluorescence ratio (R/G; green excited at
554 488 nm and collected at $\sim 530/30$ nm, red excited at 561 nm and collected at
555 $\sim 610/20$ nm). The top 30% (“high-ratio”) and bottom 30% (“low-ratio”) fractions were
556 collected. Sorted cells were pelleted at $500 \times g$ for 5 min, and genomic DNA was
557 extracted using the TIANamp Genomic DNA Kit (Tiangen, DP304-03) according to
558 the manufacturer’s instructions. sgRNA cassettes were PCR-amplified with adapter
559 primers using Phanta Flash Master Mix (Vazyme, P520) to generate sequencing-ready
560 products. PCR products were purified with Hieff NGS® DNA Selection Beads V2
561 (YEASEN, 12418ES08) and subjected to next-generation sequencing.

562

563 The MAGeCK-iNC pipeline was used to evaluate sgRNA- and gene-level phenotypes
564 relative to non-targeting controls³³. Raw sequencing reads were trimmed and aligned
565 using publicly available custom scripts from the Kampmann Lab
566 (<https://kampmannlab.ucsf.edu/resources>). Phenotype scores and p-values for target
567 genes and non-targeting controls were computed using the Mann–Whitney U test. Hit
568 genes were defined using an empirical false discovery rate (FDR) threshold of 0.01
569 (Table S2).

570

571 **sgRNA cloning**

572 Individual sgRNAs were synthesized and cloned into the pLG15 vector using the BstXI
573 and Bpu1102I restriction sites as previously described²⁷. The pLG15 vector contains a
574 mouse U6 promoter driving sgRNA expression, and an EF1 α promoter that drives
575 puromycin resistance cassette and BFP for selection. Constructs were verified by
576 Sanger sequencing. Individual sgRNAs used in this study are listed in Table S5.

577

578 **RNA extraction and quantitative real-time PCR**

579 Total RNA was isolated with the MolPure® Cell RNA Kit (Yeasen, 19231ES50)
580 following the manufacturer's instructions. Reverse transcription was carried out using
581 the HiScript III 1st Strand cDNA Synthesis Kit (Vazyme, R312). Quantitative real-time
582 PCR was performed on an FDQ-96A real-time fluorescence detection system using
583 AceQ qPCR SYBR Green Master Mix (Vazyme, CQ111-02) according to the
584 supplier's protocol. GAPDH served as the endogenous normalization control. Primers
585 used in this study are listed in Table S5.

586

587 **CRISPR-mediated gene knockout**

588 sgRNAs targeting TMEM50A exon 1 were designed using CHOPCHOP⁷⁴ and cloned
589 into pX459 (Addgene #62988). Constructs were verified by Sanger sequencing. hiPSCs
590 were transfected using Lipofectamine™ Stem (Invitrogen, STEM00003); HEK293T
591 cells were transfected with PEI (Yeasen, 40816ES01). At 48 h post-transfection, cells
592 were selected with puromycin, recovered for 48 h, and genotyped. Editing efficiency
593 was assessed by ICE (Synthego). For clonal isolation, 250 cells were seeded on
594 Matrigel-coated 35-mm dishes; colonies were manually picked into 48-well plates for
595 expansion and genotyping.

596

597 **CRISPR-mediated endogenous knock-in**

598 An sgRNA targeting the desired knock-in site was cloned into pX459 (Addgene
599 #62988). A dsDNA donor containing microhomology arms flanking the cut site, a
600 3 \times FLAG tag, and a fluorescent protein cassette was co-transfected using Hieff Trans
601 (Yeasen, 40802ES02) for HEK293T cells or Lipofectamine™ Stem (Invitrogen,

602 STEM00003) for hiPSCs. Puromycin (2 μ g/mL) was applied 48 h post-transfection for
603 72 h, followed by recovery. Fluorescent-positive cells were single-cell sorted (BD
604 FACSaria SORP) into 96-well plates (one cell per well). After \sim 2 weeks, clones were
605 genotyped by PCR and validated by Sanger sequencing.

606

607 **Electrophysiology**

608 EPSC recording was performed as described previously ^{75,76}. Electrodes had a
609 resistance of 4-5 $M\Omega$ when filled with the pipette solution, which contained: 140 mM
610 KCl, 0.5 mM EGTA, 5 mM HEPES and 3 mM Mg-ATP (pH 7.4 with KOH). The
611 extracellular solution contained: 140 mM NaCl, 3 mM KCl, 2 mM MgCl₂, 2 mM CaCl₂,
612 10 mM HEPES (pH 7.4 with NaOH). The whole-cell recording configuration was
613 obtained in voltage clamp mode with an EPC-10 amplifier (HEKA) at a sampling rate
614 of 20 kHz. For action potential (AP) recording, APs were evoked by a set of stepped
615 increasing currents (-20 to 120 pA, 300 ms; in increments of 10 pA) (PMID: 40750771).

616

617 **Immunoprecipitation-Mass Spectrometry (IP-MS)**

618 *TMEM50A* knock-in iNeurons were cultured on twelve 15-cm dishes (3×10^7
619 cells/dish). On Day 21, neurons were washed twice with ice-cold DPBS and scraped
620 into DPBS. Cells were resuspended in 2 mL lysis buffer and lysed on ice for 30 min
621 with occasional vortexing. Lysates were clarified at 14,000 rpm for 10 min at 4 °C.
622 To 1 mL clarified lysate, 80 μ L BeyoMag Anti-FLAG beads (Beyotime, P2115) and
623 80 μ L BeyoMag Mouse IgG beads (Beyotime, P2171) were added and rotated
624 overnight at 4 °C. Beads were collected, washed twice with TBST (TBS + 0.1% Tween-
625 20), and bound proteins were eluted and analyzed by SDS-PAGE followed by MS to
626 identify *TMEM50A* interactors (Table S3).

627

628 **Western blot**

629 Cells were collected and washed with cold DPBS. Cells were lysed with lysis buffer
630 (1% DDM, 150 mM HEPES, [pH 7.4], 150 mM NaCl) supplemented with EDTA-free
631 protease inhibitor cocktail (Epizyme, GRF101) on ice for 30 min. The soluble fractions

632 of cell lysates were isolated by centrifugation at 15,000 rpm for 10 min at 4 °C. Proteins
633 were denatured by the addition of 5 × SDS sampling buffer and no boiling. Samples
634 were subjected to SDS-PAGE and immunoblotting analysis.

635

636 **Co-immunoprecipitation (Co-IP)**

637 HEK293T cells were plated on a 10 cm dish for 24 h before transfection with
638 pcDNA3.1-GFP, pcDNA3.1-TMEM50A-GFP, pcDNA3.1-LEPROTL1-myc-mRuby,
639 or pcDNA3.1-CHMP4B-V5-BFP. After 48 h, cells were lysed in lysis buffer, and the
640 lysates were centrifuged at 15,000 rpm for 10 minutes at 4°C. The supernatant was
641 incubated with ABM® Anti-GFP VHH Agarose (ABMagic, MA108) or ABM® Anti-
642 MYC VHH Magarose (ABMagic, MA105) at 4°C overnight. After washing, the beads
643 were denatured and analyzed by immunoblotting.

644

645 **EGFR degradation assay**

646 HEK293T cells were seeded at 0.5×10^6 cells per well into five wells of a 12-well plate
647 and incubated for 24 h at 37 °C, 5% CO₂. The medium was then replaced with serum-
648 and antibiotic-free DMEM, and cells were serum-starved overnight. Cells were washed
649 twice with DPBS, then 0.5mL of EGF-containing DMEM (200 ng/ml) was added per
650 well. Plates were incubated at 37 °C, 5% CO₂ for 0, 20, 40, 80, and 120 min. At each
651 time point, medium was aspirated, and cells were detached with trypsin, collected, and
652 centrifuged at 200 × g for 5 min. Pellets were washed three times with DPBS and the
653 final pellet was used for lysis. Cells were lysed on ice for 30 min in 100 µL lysis buffer
654 (1% NP-40, 200 mM NaCl, 50 mM Tris-HCl, pH 8.0; optionally supplemented with
655 protease/phosphatase inhibitors). Lysates were clarified, resolved by SDS-PAGE, and
656 analyzed by immunoblotting with antibodies against EGFR (Cell Signaling Technology,
657 4267S) and GAPDH (Proteintech, HRP-60004).

658

659 **Surface Biotinylation Assay**

660 Cell surface biotinylation was performed using the Pierce™ Cell Surface Protein
661 Biotinylation Kit according to the manufacturer's instructions. WT and *TMEM50A* KO

662 iNeurons were rinsed with DPBS and incubated with 0.125 mg/mL EZ-Link™ Sulfo-
663 NHS-SS-Biotin (membrane-impermeable) in DPBS for 1 h at room temperature. The
664 reaction was quenched with 50 mM glycine for 10 min. Cells were washed three times
665 with ice-cold PBS, harvested, and lysed in 1 mL lysis buffer supplemented with a
666 complete protease inhibitor cocktail. Lysates were clarified by centrifugation at 15,000
667 $\times g$ for 10 min at 4 °C, and protein concentrations were determined by BCA assay. A
668 total of 500 μ g protein was incubated with 60 μ L NeutrAvidin agarose resin (Thermo
669 Scientific) overnight at 4 °C with gentle agitation. Resin was washed three times with
670 TBST, and biotinylated proteins were eluted using the kit elution buffer.

671

672 **Cholera toxin subunit B (CTxB) assay**

673 CTxB trafficking assay was performed as described previously⁷⁷. HEK293T cells were
674 incubated with cholera toxin subunit B (CTxB; 1:1000 in culture medium) for 5 min at
675 37 °C. Coverslips were washed and chased for 1 h, then cells were washed with PBS
676 and fixed with 4% paraformaldehyde (PFA) for 10 min. Cells were immunostained for
677 the Golgi marker GM130. Retrograde transport of CTxB was quantified by calculating
678 the Pearson's colocalization coefficient between CTxB and GM130 in Fiji (ImageJ,
679 NIH).

680

681 **Immunocytochemistry**

682 The immunocytochemistry experiments were conducted as previously described⁷⁸.
683 Briefly, cultured neurons on DIV14 were fixed with 4% paraformaldehyde (leagene
684 #DF0135), permeabilised with 0.3% Triton X-100(Solarbio #T8200) for 20 minutes
685 and blocked with 5% BSA (Solarbio #A8010) for 30 minutes. Cells were incubated
686 with primary antibodies at 4 °C overnight, followed by incubation with fluorophore-
687 conjugated secondary antibodies at room temperature for 2 hours, and coverslips were
688 mounted using Fluoromount-G (Southern Biotech #0100-01). Images were acquired
689 using a Zeiss LSM900 confocal microscope using identical acquisition settings across
690 conditions. Z-stacks were collected at 0.5 mm intervals and maximum-intensity
691 projections were used for quantification. The subsequent primary antibodies were used:

692 Guinea pig anti-MAP2 (1:1000 dilution, SYSY #SYS-188-004), Rabbit anti-MAP2
693 (1:1000 dilution; SYSY; Cat# 188 002), Chicken anti-synapsin 1/2 (1:500 dilution,
694 SYSY #106006), Mouse anti-PSD95 (1:500 dilution, Thermo MA1-046). Secondary
695 antibodies included Goat anti-guinea pig IgG Alexa FluorTM 647 (Invitrogen#A-21450),
696 Goat anti-mouse IgG Alexa FluorTM 488 (Abcam #ab150113), Goat anti-Chicken IgY
697 Alexa FluorTM 488 (Thermo #A32931).Goat anti-rabbit IgG Alexa Fluor 647 (1:500
698 dilution; Sangon; Cat# D110078), Goat anti-mouse IgG Alexa Fluor 555 (1:1000
699 dilution; Thermo; Cat# A-21428), Goat anti-chicken IgG Alexa Fluor 488 (1:500
700 dilution; Sangon; Cat# D110061).

701

702 **Scanning electron microscopy (SEM)**

703 6-week-old C57BL/6 wild-type (n = 3) and TMEM50A-KO mice (n = 3) were used for
704 SEM analysis. Mice were transcardially perfused first with ice-cold phosphate-buffered
705 saline (PBS), followed by ice-cold fixative consisting of 4% paraformaldehyde and 1%
706 glutaraldehyde in 0.1 M phosphate buffer (pH 7.2–7.4). The anterior cingulate cortex
707 (ACC) was dissected using a brain matrix (RWD #68713) and cut into approximately
708 1 × 1 × 1 mm³ blocks. Tissue samples were further fixed in 2.5% glutaraldehyde at
709 room temperature for 2 h and then overnight at 4 °C. Subsequent sample processing
710 was performed by the Bioimaging Core Facility of Shenzhen Bay Laboratory according
711 to standard protocols. Images were acquired using a Zeiss Gemini 1 360 scanning
712 electron microscope. SEM images were acquired at an accelerating voltage of 3.0 kV
713 with a working distance of approximately 5.3 mm using a backscattered electron
714 detector (Volume BSD), at a magnification of 10,000× and a resolution of 4,096 × 3,072
715 pixels.

716

717 **Animal behavior**

718 ***Contextual fear conditioning***

719 Contextual fear conditioning was performed as previously described¹³. Mice were
720 handled for 3 min per day for three consecutive days prior to training. On each
721 experimental day, mice were transferred to the behavioral testing room and allowed to

722 acclimate for at least 30 min before the session. Training was conducted in a fear-
723 conditioning chamber (25 × 25 × 25 cm) equipped with a stainless-steel grid floor
724 (Panlab, Harvard Apparatus) and maintained at 23–25 °C. All sessions were performed
725 during the dark phase of the light/dark cycle and controlled using FREEZING and
726 STARTLE software (Panlab, Harvard Apparatus). During encoding training, mice were
727 allowed to freely explore the context for 3 min, followed by delivery of three-foot
728 shocks (0.5 mA, 2 s) through the grid floor at 180 s, 242 s, and 304 s. Each shock was
729 followed by a 60 s post-shock interval. Mice were removed from the chamber 60 s after
730 the final shock and returned to their home cages. Chambers were thoroughly cleaned
731 by 75% ethanol between animals. For retrieval testing, mice were re-exposed to the
732 same context without shock for a 3-min session either 1 day (recent retrieval) or 16
733 days (remote retrieval) after training. Freezing behaviour was quantified automatically
734 using the software, defined as immobility below a threshold of 4 arbitrary units (AU)
735 for a minimum duration of 500 ms. The percentage of freezing was calculated over the
736 entire 3-min test session.

737

738 ***Open field test***

739 Open field test was conducted as previously described ⁷⁹. Mice were transferred to the
740 behavioral testing room and allowed to acclimate for at least 30 min before the test.
741 Mice were then individually placed in the center of an open field arena (RWD #63008,
742 gray acrylic, 400 × 400 × 400 mm) and allowed to explore for 10 min. Total distance
743 and time in central zone was automatically recorded by the SMARTPREMIUM Panlab
744 Explore system (v3.0). The central zone was defined as a 16 × 16 cm area. Tests were
745 performed under dim conditions (lights off) and maintained at 23–25 °C during the dark
746 phase of the light/dark cycle, and the arena was thoroughly cleaned by 75% ethanol
747 between trials.

748

749 ***Rotarod test***

750 Rotarod tests were performed similarly as previously described ⁸⁰. Mice were
751 transferred to the behavioral testing room and allowed to acclimate for at least 30 min

752 before the session. Mice were first trained on the rotating rod at 5 rpm for 3 trials with
753 10 minutes intervals. Mice were first trained on a rotarod apparatus (Panlab Harvard
754 Apparatus #LE8505, rod length 60 mm) at a constant speed of 5 rpm for three trials,
755 with 10-min inter-trial intervals. Testing was then performed with an initial speed of 4
756 rpm that accelerated linearly to 40 rpm over 300 s. Each mouse underwent three test
757 trials with 1-h inter-trial intervals, and the time latency to fall and the speed at the time
758 to fall were automatically recorded by the system and the mean was used for analysis.
759 The rod was cleaned thoroughly cleaned by 75% ethanol between animals.

760

761 **QUANTIFICATION AND STATISTICAL ANALYSIS**

762 All data were analyzed using GraphPad Prism 10 (GraphPad Software Inc.). Statistical
763 comparisons between two groups were performed using Student's t test, and
764 comparisons involving three or more groups were performed using one-way or two-
765 way ANOVA with appropriate corrections for multiple comparisons. p values < 0.05,
766 0.01, and 0.001 were considered statistically significant and are denoted by *, **, and
767 ***, respectively. Sample sizes and statistical methods for each quantification are
768 provided in the figure legends.

769

770 **Reference**

771

772 1. Peters, H.C., Hu, H., Pongs, O., Storm, J.F., and Isbrandt, D. (2005). Conditional
773 transgenic suppression of M channels in mouse brain reveals functions in neuronal
774 excitability, resonance and behavior. *Nat. Neurosci.* 8, 51–60.
775 <https://doi.org/10.1038/nn1375>.

776

777 2. Andersen, O.M., Monti, G., Jensen, A.M.G., Waal, M.W.J. de, Hulsman, M., Olsen,
778 J.G., and Holstege, H. (2024). Basic Science and Pathogenesis. *Alzheimer's Dement. : J. Alzheimer's Assoc.* 20 Suppl 1, e084835. <https://doi.org/10.1002/alz.084835>.

779

780 3. Le, S., Menacho, C., and Prigione, A. (2024). Balancing neuronal activity to fight
781 neurodevelopmental disorders. *Trends Neurosci.* 47, 241–242.
<https://doi.org/10.1016/j.tins.2024.03.002>.

782

783 4. Smith, R.S., and Walsh, C.A. (2020). Ion Channel Functions in Early Brain
784 Development. *Trends Neurosci.* 43, 103–114.
<https://doi.org/10.1016/j.tins.2019.12.004>.

785

786 5. Sun, A.X., Yuan, Q., Fukuda, M., Yu, W., Yan, H., Lim, G.G.Y., Nai, M.H.,
787 D'Agostino, G.A., Tran, H.-D., Itahana, Y., et al. (2019). Potassium channel
788 dysfunction in human neuronal models of Angelman syndrome. *Science* 366, 1486–
[1492. https://doi.org/10.1126/science.aav5386](https://doi.org/10.1126/science.aav5386).

789

790 6. Tyagi, S., Higerd-Rusli, G.P., Akin, E.J., Waxman, S.G., and Dib-Hajj, S.D. (2025).
791 Sculpting excitable membranes: voltage-gated ion channel delivery and distribution.
Nat. Rev. Neurosci. 26, 313–332. <https://doi.org/10.1038/s41583-025-00917-2>.

792

793 7. Shah, M.M., Hammond, R.S., and Hoffman, D.A. (2010). Dendritic ion channel
794 trafficking and plasticity. *Trends Neurosci.* 33, 307–316.
<https://doi.org/10.1016/j.tins.2010.03.002>.

795

796 8. Imbrici, P., Jaffe, S.L., Eunson, L.H., Davies, N.P., Herd, C., Robertson, R.,
797 Kullmann, D.M., and Hanna, M.G. (2004). Dysfunction of the brain calcium channel
798 CaV2.1 in absence epilepsy and episodic ataxia. *Brain* 127, 2682–2692.
<https://doi.org/10.1093/brain/awh301>.

799

800 9. Aarts, M., Liu, Y., Liu, L., Besshoh, S., Arundine, M., Gurd, J.W., Wang, Y.-T.,
801 Salter, M.W., and Tymianski, M. (2002). Treatment of Ischemic Brain Damage by
802 Perturbing NMDA Receptor- PSD-95 Protein Interactions. *Science* 298, 846–850.
<https://doi.org/10.1126/science.1072873>.

803

804 10. Yap, E.-L., and Greenberg, M.E. (2018). Activity-Regulated Transcription:
805 Bridging the Gap between Neural Activity and Behavior. *Neuron* 100, 330–348.
<https://doi.org/10.1016/j.neuron.2018.10.013>.

806 11. Das, S., Lituma, P.J., Castillo, P.E., and Singer, R.H. (2023). Maintenance of a
807 short-lived protein required for long-term memory involves cycles of transcription and
808 local translation. *Neuron* 111, 2051-2064.e6.
809 <https://doi.org/10.1016/j.neuron.2023.04.005>.

810 12. Sun, W., Liu, Z., Jiang, X., Chen, M.B., Dong, H., Liu, J., Südhof, T.C., and Quake,
811 S.R. (2024). Spatial transcriptomics reveal neuron–astrocyte synergy in long-term
812 memory. *Nature* 627, 374–381. <https://doi.org/10.1038/s41586-023-07011-6>.

813 13. Chen, M.B., Jiang, X., Quake, S.R., and Südhof, T.C. (2020). Persistent
814 transcriptional programmes are associated with remote memory. *Nature* 587, 437–442.
815 <https://doi.org/10.1038/s41586-020-2905-5>.

816 14. Bahl, E., Chatterjee, S., Mukherjee, U., Elsadany, M., Vanrobaeys, Y., Lin, L.-C.,
817 McDonough, M., Resch, J., Giese, K.P., Abel, T., et al. (2024). Using deep learning to
818 quantify neuronal activation from single-cell and spatial transcriptomic data. *Nat. Commun.* 15, 779. <https://doi.org/10.1038/s41467-023-44503-5>.

820 15. Yamashita, K., Kinoshita, F.L., Yoshida, S.Y., Matsumoto, K., Mitani, T.T.,
821 Fujishima, H., Minami, Y., Morii, E., Yamada, R.G., Okada, S., et al. (2025). A whole-
822 brain single-cell atlas of circadian neural activity in mice. *Science*, eaea3381.
823 <https://doi.org/10.1126/science.aea3381>.

824 16. Fuzik, J., Zeisel, A., Máté, Z., Calvignoni, D., Yanagawa, Y., Szabó, G., Linnarsson,
825 S., and Harkany, T. (2016). Integration of electrophysiological recordings with single-
826 cell RNA-seq data identifies neuronal subtypes. *Nat. Biotechnol.* 34, 175–183.
827 <https://doi.org/10.1038/nbt.3443>.

828 17. Gao, Y., Dong, Q., Arachchilage, K.H., Risgaard, R.D., Syed, M., Sheng, J.,
829 Schmidt, D.K., Jin, T., Liu, S., Sandoval, S.O., et al. (2025). Multimodal analyses reveal
830 genes driving electrophysiological maturation of neurons in the primate prefrontal
831 cortex. *Neuron*. <https://doi.org/10.1016/j.neuron.2025.04.025>.

832 18. Sterin, I., Santos, A.C., and Park, S. (2022). Neuronal Activity Reporters as Drug
833 Screening Platforms. *Micromachines-basel* 13, 1500.
834 <https://doi.org/10.3390/mi13091500>.

835 19. Lee, D., Hyun, J.H., Jung, K., Hannan, P., and Kwon, H.-B. (2017). A calcium- and
836 light-gated switch to induce gene expression in activated neurons. *Nat. Biotechnol.* 35,
837 858–863. <https://doi.org/10.1038/nbt.3902>.

838 20. Grienberger, C., and Konnerth, A. (2012). Imaging Calcium in Neurons. *Neuron*
839 73, 862–885. <https://doi.org/10.1016/j.neuron.2012.02.011>.

840 21. Fosque, B.F., Sun, Y., Dana, H., Yang, C.-T., Ohyama, T., Tadross, M.R., Patel, R.,
841 Zlatic, M., Kim, D.S., Ahrens, M.B., et al. (2015). Neural circuits. Labeling of active
842 neural circuits in vivo with designed calcium integrators. *Sci. (N. York, NY)* 347, 755–
843 760. <https://doi.org/10.1126/science.1260922>.

844 22. Edwards, K.A., Hoppa, M.B., and Bosco, G. (2020). The Photoconvertible
845 Fluorescent Probe, CaMPARI, Labels Active Neurons in Freely-Moving Intact Adult
846 Fruit Flies. *Front. Neural Circuits* 14, 22. <https://doi.org/10.3389/fncir.2020.00022>.

847 23. Moeyaert, B., Holt, G., Madangopal, R., Perez-Alvarez, A., Fearey, B.C.,
848 Trojanowski, N.F., Ledderose, J., Zolnik, T.A., Das, A., Patel, D., et al. (2018).
849 Improved methods for marking active neuron populations. *Nat. Commun.* 9, 4440.
850 <https://doi.org/10.1038/s41467-018-06935-2>.

851 24. Zolnik, T.A., Sha, F., Johenning, F.W., Schreiter, E.R., Looger, L.L., Larkum, M.E.,
852 and Sachdev, R.N.S. (2016). All-optical functional synaptic connectivity mapping in
853 acute brain slices using the calcium integrator CaMPARI. *J. Physiol.* 595, 1465–1477.
854 <https://doi.org/10.1113/jp273116>.

855 25. Trojanowski, N.F., Bottorff, J., and Turrigiano, G.G. (2021). Activity labeling
856 in vivo using CaMPARI2 reveals intrinsic and synaptic differences between neurons
857 with high and low firing rate set points. *Neuron* 109, 663-676.e5.
858 <https://doi.org/10.1016/j.neuron.2020.11.027>.

859 26. Das, A., Holden, S., Borovicka, J., Icardi, J., O’Niel, A., Chaklai, A., Patel, D., Patel,
860 R., Petrie, S.K., Raber, J., et al. (2023). Large-scale recording of neuronal activity in
861 freely-moving mice at cellular resolution. *Nat. Commun.* 14, 6399.
862 <https://doi.org/10.1038/s41467-023-42083-y>.

863 27. Tian, R., Gachechiladze, M.A., Ludwig, C.H., Laurie, M.T., Hong, J.Y., Nathaniel,
864 D., Prabhu, A.V., Fernandopulle, M.S., Patel, R., Abshari, M., et al. (2019). CRISPR
865 Interference-Based Platform for Multimodal Genetic Screens in Human iPSC-Derived
866 Neurons. *Neuron* 104, 239-255.e12. <https://doi.org/10.1016/j.neuron.2019.07.014>.

867 28. Wang, C., Ward, M.E., Chen, R., Liu, K., Tracy, T.E., Chen, X., Xie, M., Sohn,
868 P.D., Ludwig, C., Meyer-Franke, A., et al. (2017). Scalable Production of iPSC-
869 Derived Human Neurons to Identify Tau-Lowering Compounds by High-Content
870 Screening. *Stem Cell Rep.* 9, 1221–1233. <https://doi.org/10.1016/j.stemcr.2017.08.019>.

871 29. Zhang, Y., Pak, C., Han, Y., Ahlenius, H., Zhang, Z., Chanda, S., Marro, S., Patzke,
872 C., Acuna, C., Covy, J., et al. (2013). Rapid Single-Step Induction of Functional
873 Neurons from Human Pluripotent Stem Cells. *Neuron* 78, 785–798.
874 <https://doi.org/10.1016/j.neuron.2013.05.029>.

875 30. Shan, X., Zhang, A., Rezzonico, M.G., Tsai, M.-C., Sanchez-Priego, C., Zhang, Y.,
876 Chen, M.B., Choi, M., López, J.M.A., Phu, L., et al. (2024). Fully defined NGN2
877 neuron protocol reveals diverse signatures of neuronal maturation. *Cell Rep. Methods*
878 4, 100858. <https://doi.org/10.1016/j.crmeth.2024.100858>.

879 31. Kosillo, P., Doig, N.M., Ahmed, K.M., Agopyan-Miu, A.H.C.W., Wong, C.D.,
880 Conyers, L., Threlfell, S., Magill, P.J., and Bateup, H.S. (2019). Tsc1-mTORC1
881 signaling controls striatal dopamine release and cognitive flexibility. *Nat. Commun.* 10,
882 5426. <https://doi.org/10.1038/s41467-019-13396-8>.

883 32. Rao, V.R., and Lowenstein, D.H. (2015). Epilepsy. *Curr. Biol.* 25, R742–R746.
884 <https://doi.org/10.1016/j.cub.2015.07.072>.

885 33. Li, W., Xu, H., Xiao, T., Cong, L., Love, M.I., Zhang, F., Irizarry, R.A., Liu, J.S.,
886 Brown, M., and Liu, X.S. (2014). MAGeCK enables robust identification of essential
887 genes from genome-scale CRISPR/Cas9 knockout screens. *Genome Biol.* 15, 554.
888 <https://doi.org/10.1186/s13059-014-0554-4>.

889 34. Oliver, K.L., Scheffer, I.E., Bennett, M.F., Grinton, B.E., Bahlo, M., and Berkovic,
890 S.F. (2023). Genes4Epilepsy: An epilepsy gene resource. *Epilepsia* 64, 1368–1375.
891 <https://doi.org/10.1111/epi.17547>.

892 35. Mattison, K.A., Tossing, G., Mulroe, F., Simmons, C., Butler, K.M., Schreiber, A.,
893 Alsadah, A., Neilson, D.E., Naess, K., Wedell, A., et al. (2022). ATP6V0C variants
894 impair V-ATPase function causing a neurodevelopmental disorder often associated
895 with epilepsy. *Brain* 146, 1357–1372. <https://doi.org/10.1093/brain/awac330>.

896 36. Bain, J.M., Cho, M.T., Telegrafi, A., Wilson, A., Brooks, S., Botti, C., Gowans, G.,
897 Autullo, L.A., Krishnamurthy, V., Willing, M.C., et al. (2016). Variants in HNRNPH2
898 on the X Chromosome Are Associated with a Neurodevelopmental Disorder in Females.
899 *Am. J. Hum. Genet.* 99, 728–734. <https://doi.org/10.1016/j.ajhg.2016.06.028>.

900 37. Suzuki, H., Yoshida, T., Morisada, N., Uehara, T., Kosaki, K., Sato, K., Matsubara,
901 K., Takano-Shimizu, T., and Takenouchi, T. (2019). De novo NSF mutations cause
902 early infantile epileptic encephalopathy. *Ann. Clin. Transl. Neurol.* 6, 2334–2339.
903 <https://doi.org/10.1002/acn3.50917>.

904 38. Schubert, J., Siekierska, A., Langlois, M., May, P., Huneau, C., Becker, F., Muhle,
905 H., Suls, A., Lemke, J.R., Kovel, C.G.F. de, et al. (2014). Mutations in STX1B,
906 encoding a presynaptic protein, cause fever-associated epilepsy syndromes. *Nat. Genet.*
907 46, 1327–1332. <https://doi.org/10.1038/ng.3130>.

908 39. Fatima, A., Hoeber, J., Schuster, J., Koshimizu, E., Maya-Gonzalez, C., Keren, B.,
909 Mignot, C., Akram, T., Ali, Z., Miyatake, S., et al. (2021). Monoallelic and bi-allelic

910 variants in NCDN cause neurodevelopmental delay, intellectual disability, and epilepsy.
911 Am. J. Hum. Genet. 108, 739–748. <https://doi.org/10.1016/j.ajhg.2021.02.015>.

912 40. Jaworski, T., Banach-Kasper, E., and Gralec, K. (2019). GSK-3 β at the Intersection
913 of Neuronal Plasticity and Neurodegeneration. Neural Plast. 2019, 4209475.
914 <https://doi.org/10.1155/2019/4209475>.

915 41. Horn, S., Au, M., Basel-Salmon, L., Bayrak-Toydemir, P., Chapin, A., Cohen, L.,
916 Elting, M.W., Graham, J.M., Gonzaga-Jauregui, C., Konen, O., et al. (2019). De novo
917 variants in PAK1 lead to intellectual disability with macrocephaly and seizures. Brain
918 142, 3351–3359. <https://doi.org/10.1093/brain/awz264>.

919 42. Horváth, R., Abicht, A., Holinski-Feder, E., Laner, A., Gempel, K., Prokisch, H.,
920 Lochmüller, H., Klopstock, T., and Jaksch, M. (2006). Leigh syndrome caused by
921 mutations in the flavoprotein (Fp) subunit of succinate dehydrogenase (SDHA). J.
922 Neurol., Neurosurg. Psychiatry 77, 74. <https://doi.org/10.1136/jnnp.2005.067041>.

923 43. Salpietro, V., Malintan, N.T., Llano-Rivas, I., Spaeth, C.G., Efthymiou, S., Striano,
924 P., Vandrovčová, J., Cutrupi, M.C., Chimenz, R., David, E., et al. (2019). Mutations in
925 the Neuronal Vesicular SNARE VAMP2 Affect Synaptic Membrane Fusion and Impair
926 Human Neurodevelopment. Am. J. Hum. Genet. 104, 721–730.
927 <https://doi.org/10.1016/j.ajhg.2019.02.016>.

928 44. Johnstone, D.L., Nguyen, T.T.M., Zambonin, J., Kernohan, K.D., St-Denis, A.,
929 Baratang, N.V., Hartley, T., Geraghty, M.T., Richer, J., Majewski, J., et al. (2020).
930 Early infantile epileptic encephalopathy due to biallelic pathogenic variants in PIGQ:
931 Report of seven new subjects and review of the literature. J. Inherit. Metab. Dis. 43,
932 1321–1332. <https://doi.org/10.1002/jimd.12278>.

933 45. Kim, K., Park, I., Kim, J., Kang, M.-G., Choi, W.G., Shin, H., Kim, J.-S., Rhee, H.-
934 W., and Suh, J.M. (2021). Dynamic tracking and identification of tissue-specific
935 secretory proteins in the circulation of live mice. Nat. Commun. 12, 5204.
936 <https://doi.org/10.1038/s41467-021-25546-y>.

937 46. Stenmark, H. (2009). Rab GTPases as coordinators of vesicle traffic. Nat. Rev. Mol.
938 Cell Biol. 10, 513–525. <https://doi.org/10.1038/nrm2728>.

939 47. Shin, J., Nile, A., and Oh, J.-W. (2021). Role of adaptin protein complexes in
940 intracellular trafficking and their impact on diseases. Bioengineered 12, 8259–8278.
941 <https://doi.org/10.1080/21655979.2021.1982846>.

942 48. Liu, Q., Bautista-Gomez, J., Higgins, D.A., Yu, J., and Xiong, Y. (2021).
943 Dysregulation of the AP2M1 phosphorylation cycle by LRRK2 impairs endocytosis
944 and leads to dopaminergic neurodegeneration. Sci. Signal. 14.
945 <https://doi.org/10.1126/scisignal.abg3555>.

946 49. Mouret, R.Z., Greenbaum, J.P., Doll, H.M., Brody, E.M., Iacobucci, E.L., Roland,
947 N.C., Simamora, R.C., Ruiz, I., Seymour, R., Ludwick, L., et al. (2024). The adaptor
948 protein 2 (AP2) complex modulates habituation and behavioral selection across
949 multiple pathways and time windows. *iScience* 27, 109455.
950 <https://doi.org/10.1016/j.isci.2024.109455>.

951 50. Howe, E.N., Burnette, M.D., Justice, M.E., Schnepp, P.M., Hedrick, V., Clancy,
952 J.W., Guldner, I.H., Lamere, A.T., Li, J., Aryal, U.K., et al. (2020). Rab11b-mediated
953 integrin recycling promotes brain metastatic adaptation and outgrowth. *Nat. Commun.*
954 11, 3017. <https://doi.org/10.1038/s41467-020-16832-2>.

955 51. Kang, H., Han, A., Zhang, A., Jeong, H., Koh, W., Lee, J.M., Lee, H., Jo, H.Y.,
956 Maria-Solano, M.A., Bhalla, M., et al. (2024). GolpHCat (TMEM87A), a unique
957 voltage-dependent cation channel in Golgi apparatus, contributes to Golgi-pH
958 maintenance and hippocampus-dependent memory. *Nat. Commun.* 15, 5830.
959 <https://doi.org/10.1038/s41467-024-49297-8>.

960 52. Stoetzel, C., Bär, S., Craene, J.-O.D., Scheidecker, S., Etard, C., Chicher, J., Reck,
961 J.R., Perrault, I., Geoffroy, V., Chennen, K., et al. (2016). A mutation in VPS15
962 (PIK3R4) causes a ciliopathy and affects IFT20 release from the cis-Golgi. *Nat.*
963 *Commun.* 7, 13586. <https://doi.org/10.1038/ncomms13586>.

964 53. Koike, S., and Jahn, R. (2019). SNAREs define targeting specificity of trafficking
965 vesicles by combinatorial interaction with tethering factors. *Nat. Commun.* 10, 1608.
966 <https://doi.org/10.1038/s41467-019-09617-9>.

967 54. Babst, M., Katzmann, D.J., Estepa-Sabal, E.J., Meerloo, T., and Emr, S.D. (2002).
968 Escrt-III An endosome-associated heterooligomeric protein complex required for mvb
969 sorting. *Dev. Cell* 3, 271–282. [https://doi.org/10.1016/s1534-5807\(02\)00220-4](https://doi.org/10.1016/s1534-5807(02)00220-4).

970 55. Azmi, I.F., Davies, B.A., Xiao, J., Babst, M., Xu, Z., and Katzmann, D.J. (2008).
971 ESCRT-III Family Members Stimulate Vps4 ATPase Activity Directly or via Vta1.
972 *Dev. Cell* 14, 50–61. <https://doi.org/10.1016/j.devcel.2007.10.021>.

973 56. Migliano, S.M., Schultz, S.W., Wenzel, E.M., Takáts, S., Liu, D., Mørk, S., Tan,
974 K.W., Rusten, T.E., Raiborg, C., and Stenmark, H. (2023). Removal of hypersignaling
975 endosomes by simaphagy. *Autophagy* 20, 769–791.
976 <https://doi.org/10.1080/15548627.2023.2267958>.

977 57. Schluter, C., Lam, K.K.Y., Brumm, J., Wu, B.W., Saunders, M., Stevens, T.H.,
978 Bryan, J., and Conibear, E. (2008). Global Analysis of Yeast Endosomal Transport
979 Identifies the Vps55/68 Sorting Complex. *Mol. Biol. Cell* 19, 1282–1294.
980 <https://doi.org/10.1091/mbc.e07-07-0659>.

981 58. Alsleben, S., and Kölling, R. (2022). Vps68 cooperates with ESCRT-III in
982 intraluminal vesicle formation. *J. Cell Sci.* *135*. <https://doi.org/10.1242/jcs.259743>.

983 59. Longva, K.E., Blystad, F.D., Stang, E., Larsen, A.M., Johannessen, L.E., and
984 Madshus, I.H. (2002). Ubiquitination and proteasomal activity is required for transport
985 of the EGF receptor to inner membranes of multivesicular bodies. *J. Cell Biol.* *156*,
986 843–854. <https://doi.org/10.1083/jcb.200106056>.

987 60. Hurley, J.H., Coyne, A.N., Miączyńska, M., and Stenmark, H. (2025). The
988 expanding repertoire of ESCRT functions in cell biology and disease. *Nature* *642*, 877–
989 888. <https://doi.org/10.1038/s41586-025-08950-y>.

990 61. Neefjes, J., Jongsma, M.M.L., and Berlin, I. (2017). Stop or Go? Endosome
991 Positioning in the Establishment of Compartment Architecture, Dynamics, and
992 Function. *Trends Cell Biol.* *27*, 580–594. <https://doi.org/10.1016/j.tcb.2017.03.002>.

993 62. Im, Y.J., Wollert, T., Boura, E., and Hurley, J.H. (2009). Structure and Function of
994 the ESCRT-II-III Interface in Multivesicular Body Biogenesis. *Dev. Cell* *17*, 234–243.
995 <https://doi.org/10.1016/j.devcel.2009.07.008>.

996 63. Stuffers, S., Wegner, C.S., Stenmark, H., and Brech, A. (2009). Multivesicular
997 Endosome Biogenesis in the Absence of ESCRTs. *Traffic* *10*, 925–937.
998 <https://doi.org/10.1111/j.1600-0854.2009.00920.x>.

999 64. Piper, R.C., and Katzmann, D.J. (2007). Biogenesis and Function of Multivesicular
1000 Bodies. *Cell Dev. Biol.* *23*, 519–547.
1001 <https://doi.org/10.1146/annurev.cellbio.23.090506.123319>.

1002 65. Bartheld, C.S.V., and Altick, A.L. (2011). Multivesicular bodies in neurons:
1003 Distribution, protein content, and trafficking functions. *Prog. Neurobiol.* *93*, 313–340.
1004 <https://doi.org/10.1016/j.pneurobio.2011.01.003>.

1005 66. Cadwell, C.R., Palasantza, A., Jiang, X., Berens, P., Deng, Q., Yilmaz, M., Reimer,
1006 J., Shen, S., Bethge, M., Tolias, K.F., et al. (2016). Electrophysiological, transcriptomic
1007 and morphologic profiling of single neurons using Patch-seq. *Nat. Biotechnol.* *34*, 199–
1008 203. <https://doi.org/10.1038/nbt.3445>.

1009 67. Vardar, G., Chang, S., Arancillo, M., Wu, Y.-J., Trimbuch, T., and Rosenmund, C.
1010 (2016). Distinct Functions of Syntaxin-1 in Neuronal Maintenance, Synaptic Vesicle
1011 Docking, and Fusion in Mouse Neurons. *J. Neurosci.* *36*, 7911–7924.
1012 <https://doi.org/10.1523/jneurosci.1314-16.2016>.

1013 68. Kölling, R. (2024). Interaction between ESCRT-III proteins and the yeast SERINC
1014 homolog Tms1. *GENETICS* *228*, iyae132. <https://doi.org/10.1093/genetics/iyae132>.

1015 69. Picon, C., Aleksynas, R., Wojewska, M., Virgiliis, F. de, Merkler, D., and Reynolds, R. (2025). Dysregulation of the endosomal sorting complex III is linked to neurodegeneration in progressive multiple sclerosis. *Brain Pathol.* *36*, e70034. <https://doi.org/10.1111/bpa.70034>.

1019 70. Coulter, M.E., Dorobantu, C.M., Lodewijk, G.A., Delalande, F., Cianferani, S., Ganesh, V.S., Smith, R.S., Lim, E.T., Xu, C.S., Pang, S., et al. (2018). The ESCRT-III Protein CHMP1A Mediates Secretion of Sonic Hedgehog on a Distinctive Subtype of Extracellular Vesicles. *Cell Rep.* *24*, 973-986.e8. <https://doi.org/10.1016/j.celrep.2018.06.100>.

1024 71. Lee, J.-A., Beigneux, A., Ahmad, S.T., Young, S.G., and Gao, F.-B. (2007). ESCRT-III Dysfunction Causes Autophagosome Accumulation and Neurodegeneration. *Curr. Biol.* *17*, 1561–1567. <https://doi.org/10.1016/j.cub.2007.07.029>.

1028 72. Boggess, S.C., Gandhi, V., Tsai, M.-C., Marzette, E., Teyssier, N., Chou, J.Y.-Y., Hu, X., Cramer, A., Yadanar, L., Shroff, K., et al. (2025). A Massively Parallel CRISPR-Based Screening Platform for Modifiers of Neuronal Activity. *bioRxiv*, 2024.02.28.582546. <https://doi.org/10.1101/2024.02.28.582546>.

1032 73. Beaudoin, G.M.J., Lee, S.-H., Singh, D., Yuan, Y., Ng, Y.-G., Reichardt, L.F., and Arikkath, J. (2012). Culturing pyramidal neurons from the early postnatal mouse hippocampus and cortex. *Nat. Protoc.* *7*, 1741–1754. <https://doi.org/10.1038/nprot.2012.099>.

1036 74. Labun, K., Montague, T.G., Krause, M., Cleuren, Y.N.T., Tjeldnes, H., and Valen, E. (2019). CHOPCHOP v3: expanding the CRISPR web toolbox beyond genome editing. *Nucleic Acids Res.* *47*, W171–W174. <https://doi.org/10.1093/nar/gkz365>.

1039 75. Zeng, Q., Li, Y., Wu, Y., Wu, J., Xu, K., Chen, Y., Rao, Y., Li, N., Luo, Y., Jiang, C., et al. (2025). Neuropeptide Y neurons mediate opioid-induced itch by disinhibiting GRP-GRPR microcircuits in the spinal cord. *Nat. Commun.* *16*, 7074. <https://doi.org/10.1038/s41467-025-62382-w>.

1043 76. Shan, L., Xu, K., Ji, L., Zeng, Q., Liu, Y., Wu, Y., Chen, Y., Li, Y., Hu, Q., Wu, J., et al. (2024). Injured sensory neurons-derived galectin-3 contributes to neuropathic pain via programming microglia in the spinal dorsal horn. *Brain, Behav., Immun.* *117*, 80–99. <https://doi.org/10.1016/j.bbi.2024.01.002>.

1047 77. Petkovic, M., Osés-Prieto, J., Burlingame, A., Jan, L.Y., and Jan, Y.N. (2020). TMEM16K is an interorganelle regulator of endosomal sorting. *Nat. Commun.* *11*, 3298. <https://doi.org/10.1038/s41467-020-17016-8>.

1050 78. Hale, W.D., Südhof, T.C., and Huganir, R.L. (2023). Engineered adhesion
1051 molecules drive synapse organization. *Proc. Natl. Acad. Sci.* *120*, e2215905120.
1052 <https://doi.org/10.1073/pnas.2215905120>.

1053 79. Kraeuter, A.-K., Guest, P.C., and Sarnyai, Z. (2018). The Open Field Test for
1054 Measuring Locomotor Activity and Anxiety-Like Behavior. *Methods Mol. Biol.*
1055 (Clifton, NJ) *1916*, 99–103. https://doi.org/10.1007/978-1-4939-8994-2_9.

1056 80. Wang, G., Peng, S., Mendez, M.R., Keramidas, A., Castellano, D., Wu, K., Han,
1057 W., Tian, Q., Dong, L., Li, Y., et al. (2024). The TMEM132B-GABAA receptor
1058 complex controls alcohol actions in the brain. *Cell* *187*, 6649-6668.e35.
1059 <https://doi.org/10.1016/j.cell.2024.09.006>.

1060 81. Hallgren, J., Tsirigos, K.D., Pedersen, M.D., Armenteros, J.J.A., Marcatili, P.,
1061 Nielsen, H., Krogh, A., and Winther, O. (2022). DeepTMHMM predicts alpha and beta
1062 transmembrane proteins using deep neural networks.
1063 <https://doi.org/10.1101/2022.04.08.487609>.

1064
1065

1066 **ACKNOWLEDGEMENTS**

1067 We thank the assistance of SUSTech Core Research Facilities on flow cytometry. We
1068 also would like to acknowledge the SZBL Bio-Imaging core for assistance with the
1069 SEM sample preparation and imaging.

1070

1071 **Funding**

1072 National Key Research and Development Program of China 2024YFA0919800 (RT)
1073 Shenzhen Medical Research Fund A2303039 (RT)
1074 Shenzhen Medical Research Fund C2301006 (ZW)
1075 Guangdong Basic and Applied Basic Research Foundation 2023B1515020075 (RT)
1076 Key Area Research and Development Program of Guangdong Province
1077 2023B0303010002 (ZW)
1078 Shenzhen Fundamental Research Program RCYX20221008092845052 (RT)
1079 Lingang Laboratory Grant LGL-3142-ADB24020 (XJ)

1080

1081 **Author contributions**

1082 Conceptualization: RT, XJ
1083 Investigation: JW, ML, YC, JC, XZ
1084 Supervision: ZW, XJ, RT
1085 Writing – original draft: JW, ML, RT
1086 Writing – review & editing: All authors.

1087

1088 **Competing interests**

1089 All other authors declare they have no competing interests.

1090

1091 **Data and materials availability**

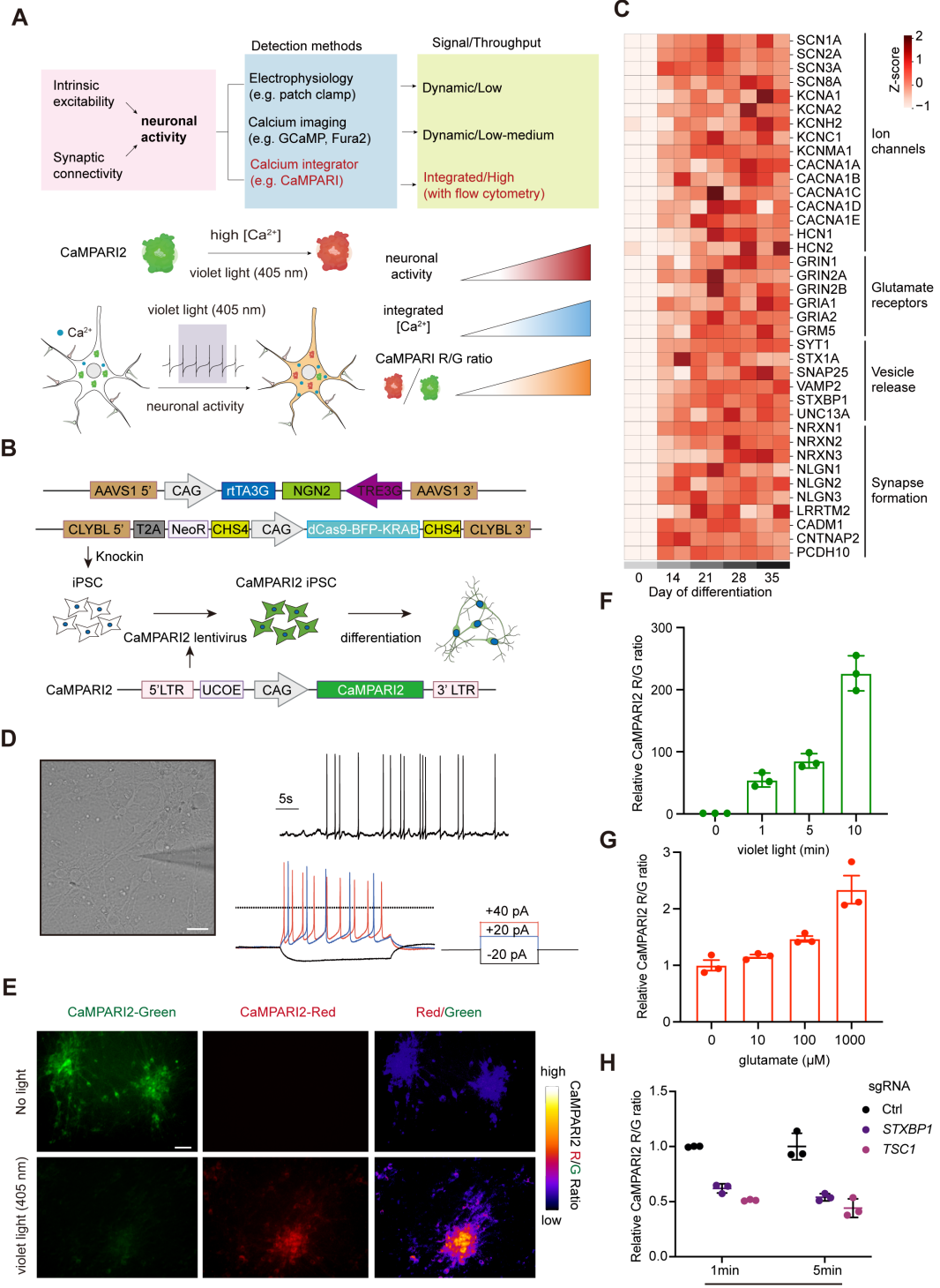
1092 All data are available in the main text or the supplementary materials.

1093

1094

1095

FIGURES AND FIGURE LEGENDS



1096

1097 **Figure 1. Establishment of a CaMPARI2-based high-throughput platform for**
 1098 **quantifying neuronal activity in human iNeurons**

1099 (A) Schematic comparison of major approaches for measuring neuronal activity.
 1100 Electrophysiology provides gold-standard but low-throughput measurements; calcium
 1101 and voltage imaging capture transient activity in low- to medium-throughput arrayed

1102 formats; CaMPARI2 converts cumulative Ca^{2+} activity during a defined illumination
1103 window into a stable red/green fluorescence ratio that can be quantified at single-cell
1104 resolution by flow cytometry, enabling pooled genetic screening.

1105 (B) Strategy for integrating CaMPARI2 into the CRISPRi iNeuron platform. Human
1106 iPSCs carry a doxycycline-inducible NGN2 cassette at the AAVS1 locus and a
1107 dCas9-BFP-KRAB cassette at the CLYBL locus. CaMPARI2 is introduced by lentiviral
1108 transduction under a CAG promoter. Upon doxycycline induction, iPSCs rapidly
1109 differentiate into glutamatergic iNeurons expressing CaMPARI2 and CRISPRi
1110 machinery.

1111 (C) Transcriptomic maturation of iNeurons. Heatmap showing expression dynamics of
1112 representative neuronal activity-related genes (including ion channels, glutamate
1113 receptors, vesicle release machinery, and synaptic components) across days 14, 21, 28,
1114 and 35 of differentiation. Expression of activity-associated genes increases after day 14
1115 and plateaus around days 21–28.

1116 (D) Functional maturation of iNeurons by electrophysiology. Left, DIC image of day
1117 28 iNeurons (scale bar, 10 μm). Right, representative traces of spontaneous (top) and
1118 evoked (bottom) action potential in day 28 iNeurons.

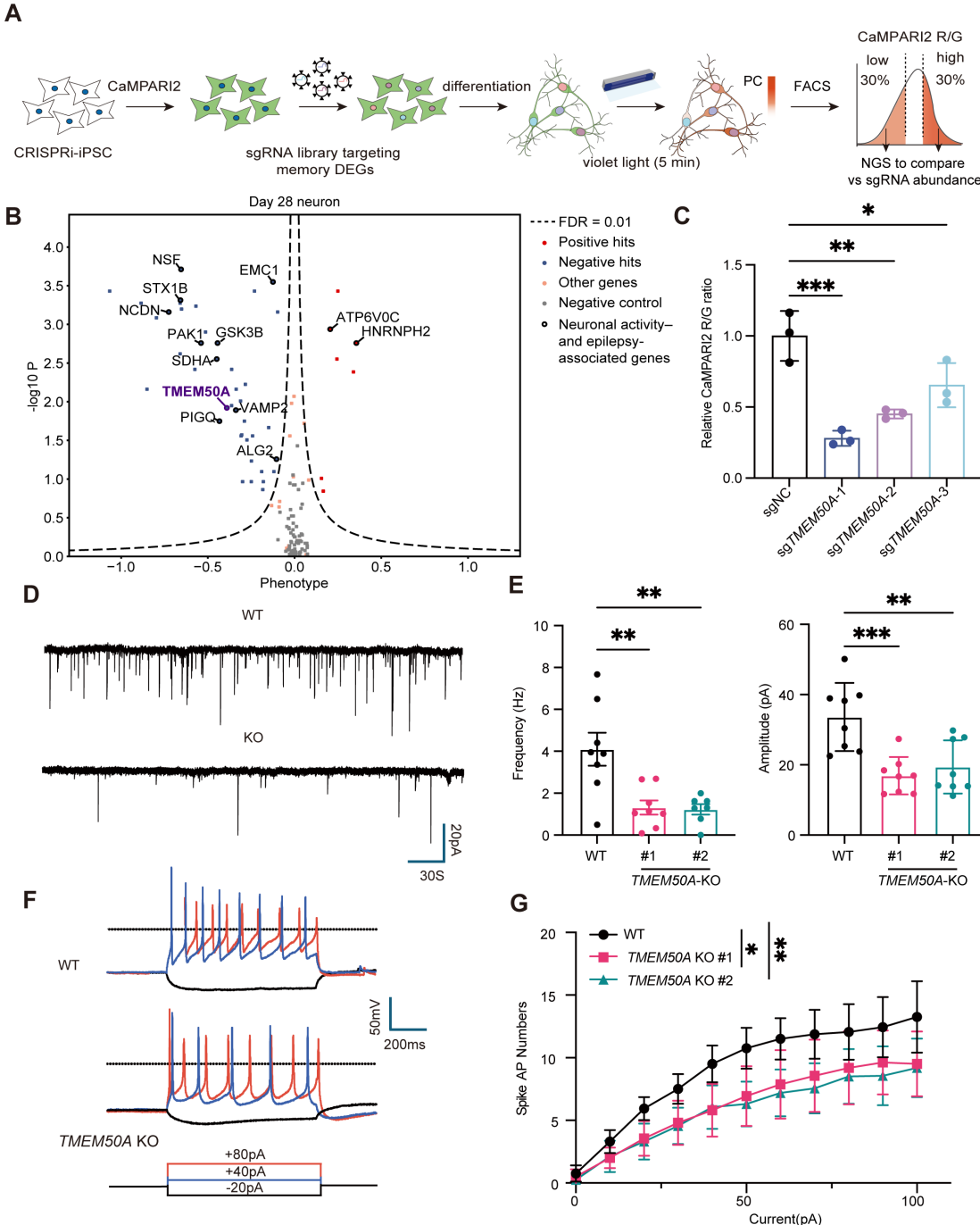
1119 (E) Representative confocal images of CaMPARI2-iNeurons before and after 5 min of
1120 405 nm violet light illumination. Panels show green fluorescence, red fluorescence, and
1121 green-to-red ratio. Scale bar: 10 μm .

1122 (F) Quantification of CaMPARI2 photoconversion by flow cytometry as a function of
1123 illumination time. CaMPARI2 red-to-green (R/G) fluorescence ratio increases with
1124 longer illumination duration (0–10 min). Data are presented as mean \pm SD. $n = 3$
1125 biological replicates per condition.

1126 (G) Dose-dependent increase in CaMPARI2 R/G ratio upon glutamate stimulation.
1127 iNeurons were treated with increasing concentrations of glutamate (0–100 μM) for 5
1128 min during violet light illumination. Data are presented as mean \pm SD. $n = 3$ biological
1129 replicates per condition.

1130 (H) CaMPARI2 detects genetically driven changes in neuronal activity. Quantification
1131 of CaMPARI2 R/G ratio in control iNeurons (NTC) versus iNeurons with CRISPRi-

1132 mediated knockdown of *TSC1* or *STXBPI* under 1 min (left) or 5 min (right)
1133 illumination. Data are presented as mean \pm SD. n = 3 biological replicates per condition.



1134

1135 **Figure 2. A CaMPARI2-based CRISPRi screen identifies TMEM50A as an**
 1136 **essential regulator of neuronal activity**

1137 (A) Schematic of the CaMPARI2-CRISPRi screening workflow. CRISPRi-iPSCs
 1138 expressing CaMPARI2 were transduced with an sgRNA library targeting memory-
 1139 associated DEGs. Following differentiation into iNeurons, cells were subjected to 5 min
 1140 of violet light photoconversion (PC), dissociated, and sorted by FACS based on
 1141 CaMPARI2 red-to-green (R/G) ratio. The top 30% (high activity) and bottom 30% (low

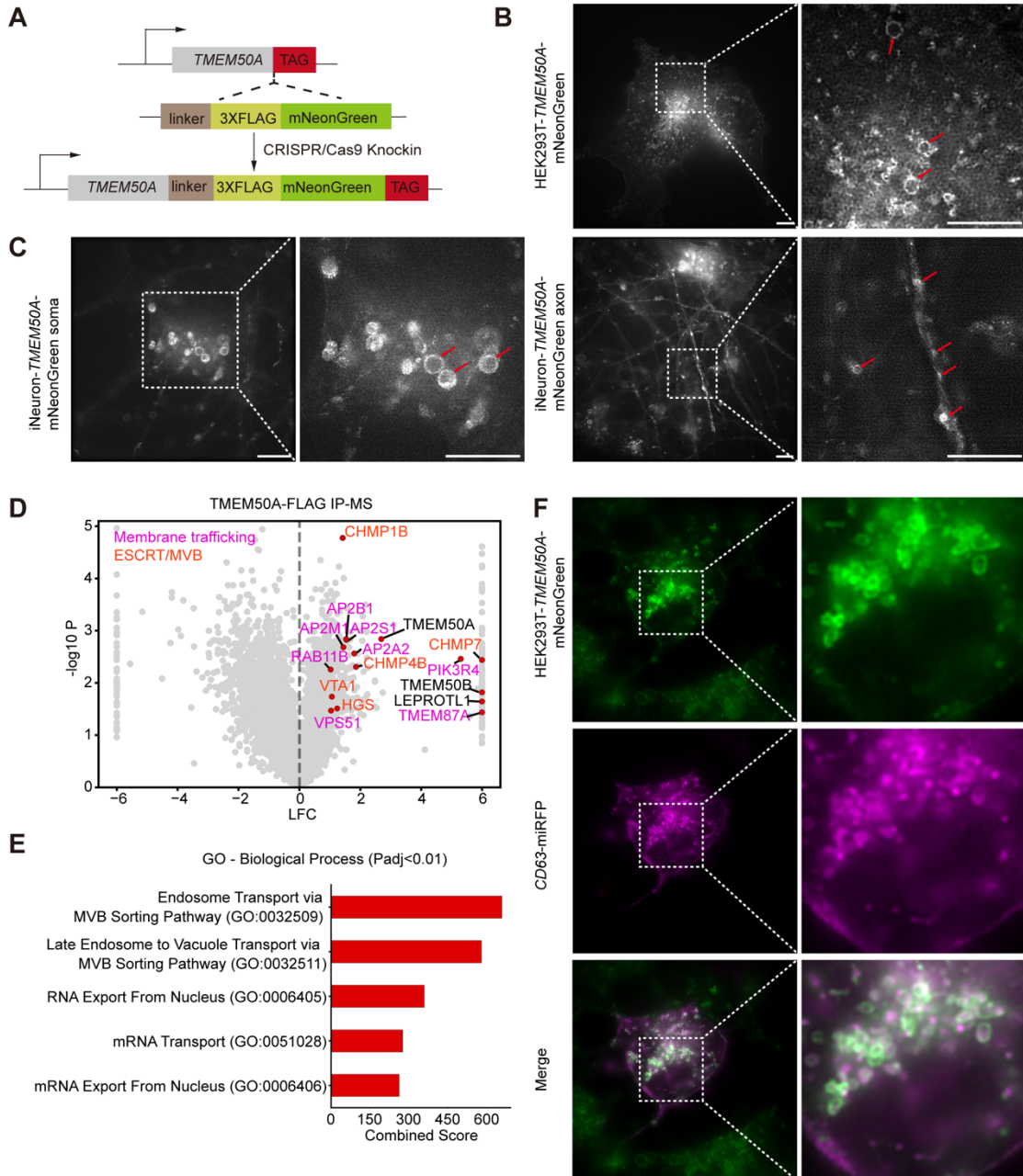
1142 activity) populations were collected, and sgRNA representation was quantified by next-
1143 generation sequencing (NGS) to identify hits.

1144 (B) Volcano plot showing the CaMPARI2 screen results. The x axis indicates the
1145 activity phenotype score (negative values, decreased CaMPARI2 signal upon
1146 knockdown; positive values, increased signal), and the y axis indicates $-\log_{10} P$ from
1147 MAGeCK-iNC analysis. Dashed line marks FDR = 0.01. Selected known neuronal
1148 activity- and epilepsy-associated genes are labeled. *TMEM50A*, a gene of previously
1149 unknown function, is highlighted in purple.

1150 (C) Validation of *TMEM50A* as a negative hit from the screen. Relative CaMPARI2
1151 R/G ratio in iNeurons transduced with non-targeting control sgRNA (sgNTC) or three
1152 independent sgRNAs targeting *TMEM50A* (sgTMEM50A-1, -2, -3). Data are
1153 normalized to sgNTC and presented as mean \pm SD (n = 3 biological replicates). *p <
1154 0.05, **p < 0.01, ***p < 0.001, one-way ANOVA.

1155 (D–E) *TMEM50A* loss impairs excitatory synaptic transmission. (D) Representative
1156 voltage-clamp traces of sEPSCs in WT and *TMEM50A* KO iNeurons. Scale bars: 20
1157 pA, 30 s. (E) Quantification of sEPSC frequency (left) and amplitude (right) in WT and
1158 two independent *TMEM50A* KO lines (#1, #2). Each dot represents one cell. Data are
1159 presented as mean \pm SEM (n = 8 neurons). *p < 0.05, **p < 0.01, ***p < 0.001, one-
1160 way ANOVA.

1161 (F–G) *TMEM50A* loss reduces intrinsic excitability. (F) Representative current-clamp
1162 recordings showing action potential firing in response to current injections (-20, +40,
1163 +80 pA; 300 ms) in WT and *TMEM50A* KO iNeurons. Scale bars: 50 mV, 200 ms. (G)
1164 Input–output curves showing the number of action potentials evoked as a function of
1165 injected current for WT and *TMEM50A* KO (#1, #2) iNeurons. Data are presented as
1166 mean \pm SEM (n = 16 neurons). *p < 0.05, **p < 0.01, Two-way ANOVA Bonferroni's
1167 multiple comparisons.



1168

1169 **Figure 3. TMEM50A localizes to multivesicular bodies**

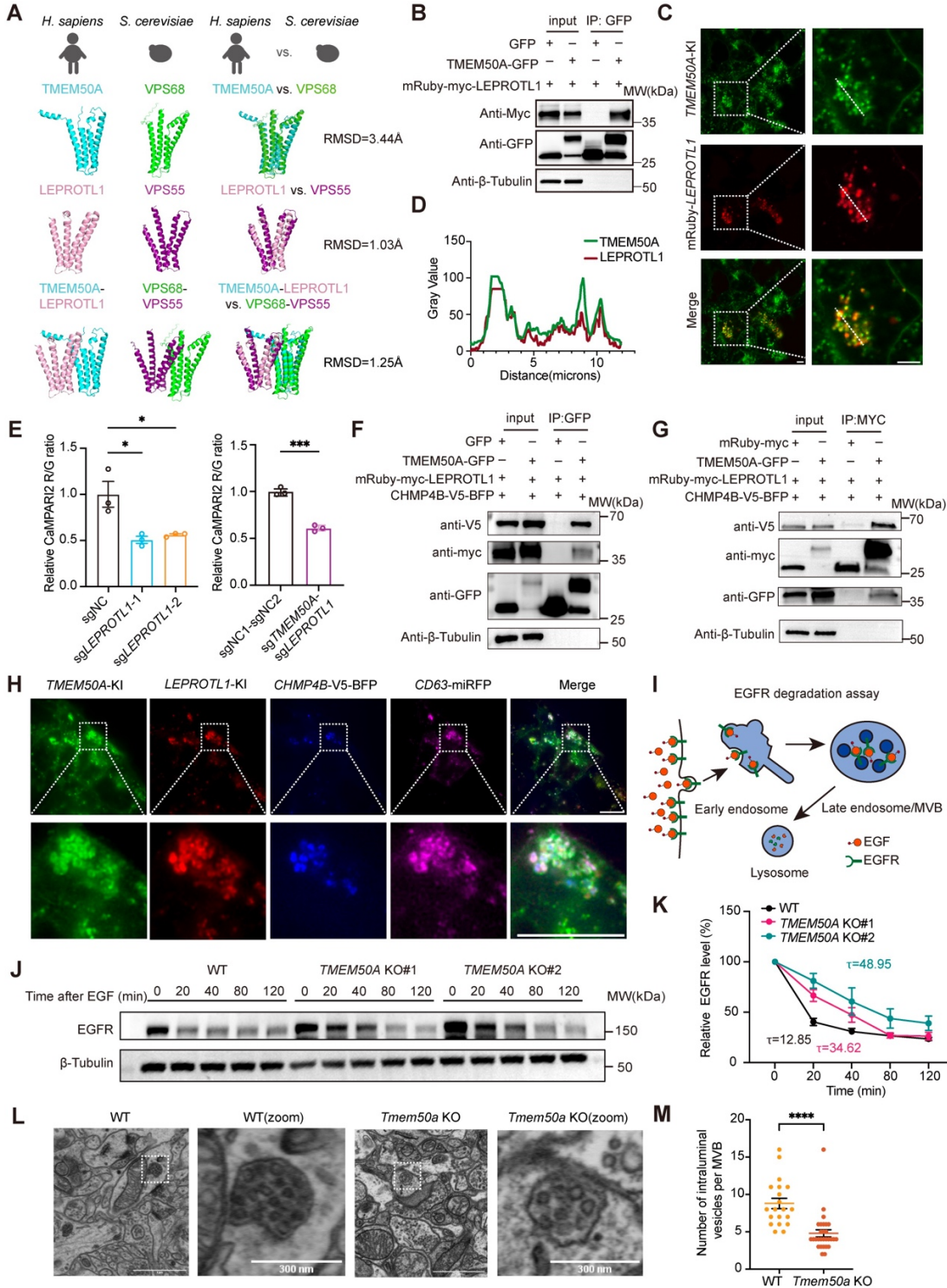
1170 (A) Schematic of CRISPR/Cas9-mediated endogenous tagging strategy. A C-terminal
 1171 3×FLAG-mNeonGreen cassette was inserted in-frame at the TMEM50A locus to
 1172 generate TMEM50A-3×FLAG-mNeonGreen knock-in (KI) cells.
 1173 (B–C) Super-resolution imaging of endogenously tagged TMEM50A-mNeonGreen.
 1174 TMEM50A shows a punctate, vesicular distribution in HEK293T KI cells and in
 1175 iNeurons, with TMEM50A-positive vesicles present in both soma and neurites.
 1176 Magnified views highlight representative TMEM50A-positive vesicles (red arrows).
 1177 Scale bars, 5 μm.

1178 (D) Volcano plot of proteins identified by TMEM50A–FLAG immunoprecipitation–
1179 mass spectrometry (IP–MS) in iNeurons. The x axis shows \log_2 fold change (LFC)
1180 relative to IgG control and the y axis shows $-\log_{10} P$. TMEM50A and selected enriched
1181 interactors involved in membrane trafficking (magenta) and ESCRT/MVB function
1182 (orange) are labeled.

1183 (E) Gene Ontology (GO) enrichment analysis of TMEM50A interactors ($P_{adj} < 0.01$).

1184 (F) Co-localization of TMEM50A with the MVB marker CD63. Representative
1185 confocal images of HEK293T TMEM50A–mNeonGreen KI cells (green) co-
1186 expressing CD63–mRFP (magenta). Scale bars, 5 μm .

1187



1188

1189 **Figure 4. TMEM50A forms a complex with LEPROT1 and ESCRT-III to**
 1190 **support MVB function**

1191 (A) Structural conservation of the TMEM50A-LEPROTL1 complex. AlphaFold3-
 1192 based models of human TMEM50A and LEPROT1 and their yeast homologs Vps68
 1193 and Vps55, shown individually and as complexes.

1194 (B) Co-immunoprecipitation (co-IP) showing interaction between TMEM50A and
1195 LEPROT1. HEK293T cells expressing TMEM50A-GFP and mRuby-myc-
1196 LEPROT1 were subjected to GFP immunoprecipitation followed by immunoblotting
1197 with anti-Myc and anti-GFP; β -tubulin, loading control.

1198 (C–D) Co-localization of TMEM50A and LEPROT1 in cells. (C) Representative
1199 fluorescence images of TMEM50A knock-in (KI) cells expressing mRuby-myc-
1200 LEPROT1; Scale bars, 5 μ m. (D) Line-scan intensity profiles across the indicated
1201 region show correlated TMEM50A and LEPROT1 signals.

1202 (E) Functional epistasis analysis. CaMPARI2 R/G ratio in iNeurons with CRISPRi-
1203 mediated knockdown of *LEPROT1* individually (left) or in combination with
1204 *TMEM50A* (right). Double knockdown does not enhance the phenotype relative to
1205 single knockdowns, indicating that TMEM50A and LEPROT1 function in the same
1206 pathway. Relative R/G ratios normalized to control sgRNA are shown as mean \pm SD (n
1207 = 3 biological replicates). * p < 0.05, ** p < 0.01, *** p < 0.001, One-way ANOVA.

1208 (F–G) Co-IP demonstrating interactions among TMEM50A, LEPROT1, and the
1209 ESCRT-III component CHMP4B. (F) Anti-GFP IP from cells co-expressing mRuby-
1210 myc, TMEM50A-GFP, mRuby-myc-LEPROT1, and CHMP4B-V5-BFP. (G) Anti-
1211 Myc IP from cells co-expressing the same constructs.

1212 (H) Co-localization of TMEM50A, LEPROT1, CHMP4B, and CD63 at MVBs.
1213 Representative confocal images of cells co-expressing TMEM50A-mNeonGreen
1214 (green), LEPROT1-mRuby (red), CHMP4B-V5-BFP (blue), and CD63-mRFP
1215 (magenta). Scale bars, 5 μ m.

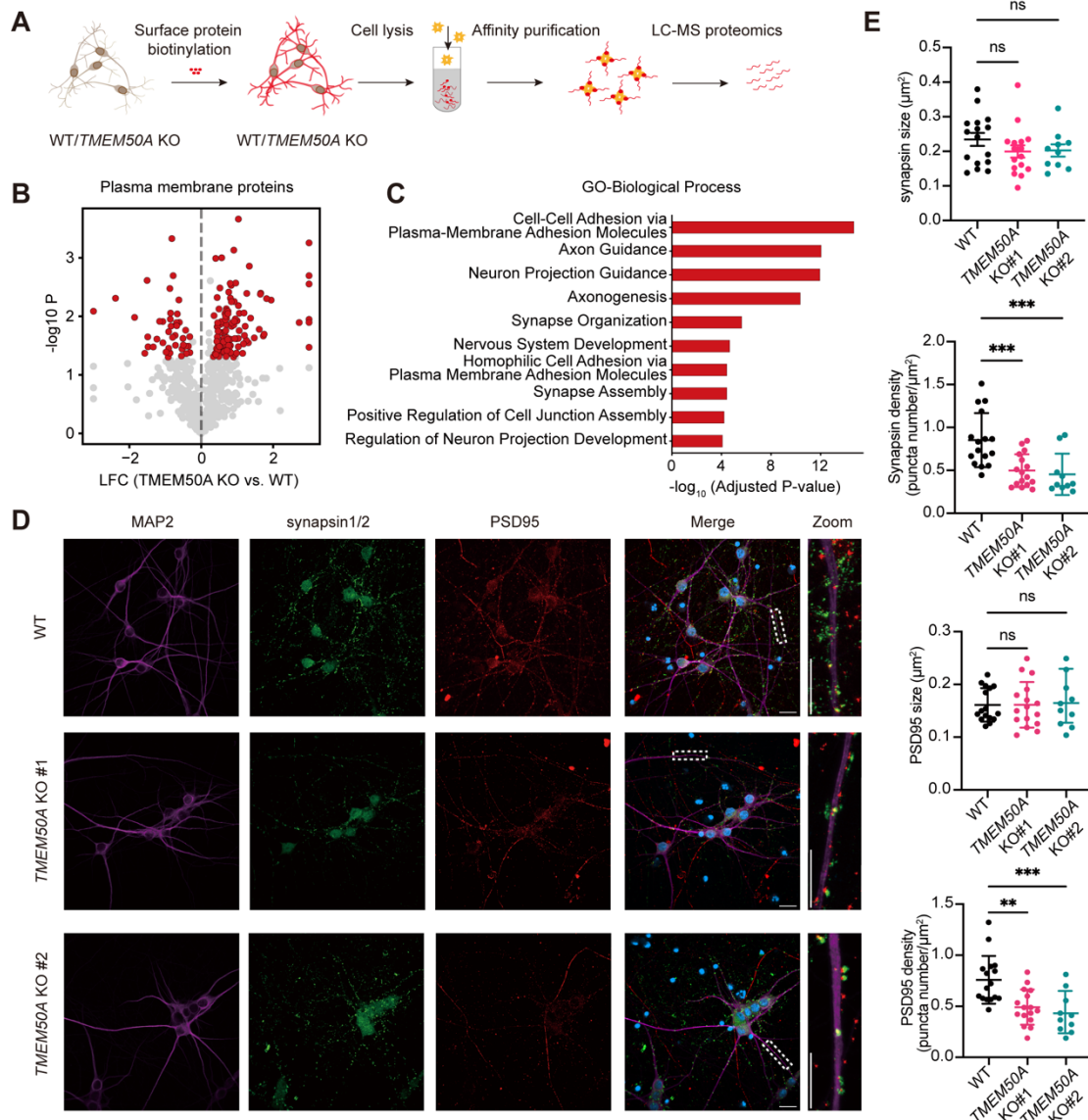
1216 (I) Schematic of the EGFR degradation assay.

1217 (J–K) TMEM50A is required for efficient EGFR degradation. (J) Time-course Western
1218 blots of EGFR levels following EGF stimulation in WT and two independent
1219 *TMEM50A* knockout (KO#1, KO#2) HEK293T cell lines; β -Tubulin serves as a loading
1220 control. (K) Quantification of relative EGFR levels (normalized to time 0) plotted over
1221 time KO cells show a slower EGFR degradation rate compared to WT cells. The decay
1222 rates (τ) for each condition are indicated on the graph. Data are presented as mean \pm
1223 SEM (n = 3 biological replicates).

1224 (L–M) *Tmem50a* loss reduces intraluminal vesicle (ILV) formation in MVBs *in vivo*.
1225 (L) Representative scanning electron microscopy (SEM) images of MVBs from the
1226 anterior cingulate cortex (ACC) of WT and *Tmem50a*-KO mice. Scale bars, as indicated.
1227 (M) Quantification of ILV number per MVB. Each dot represents one MVB; Data are
1228 presented as mean \pm SEM (WT: n = 20; *Tmem50a*-KO: n = 29). ***p < 0.0001, one-
1229 way ANOVA.

1230

1231



1232

1233 **Figure 5. TMEM50A loss remodels the neuronal surface proteome and reduces**
1234 **synapse density in human iNeurons**

1235 (A) Schematic of the surface proteomics workflow. WT and *TMEM50A* KO iNeurons
1236 were subjected to cell-surface protein biotinylation, followed by cell lysis, affinity
1237 purification of biotinylated proteins, and LC-MS/MS analysis.

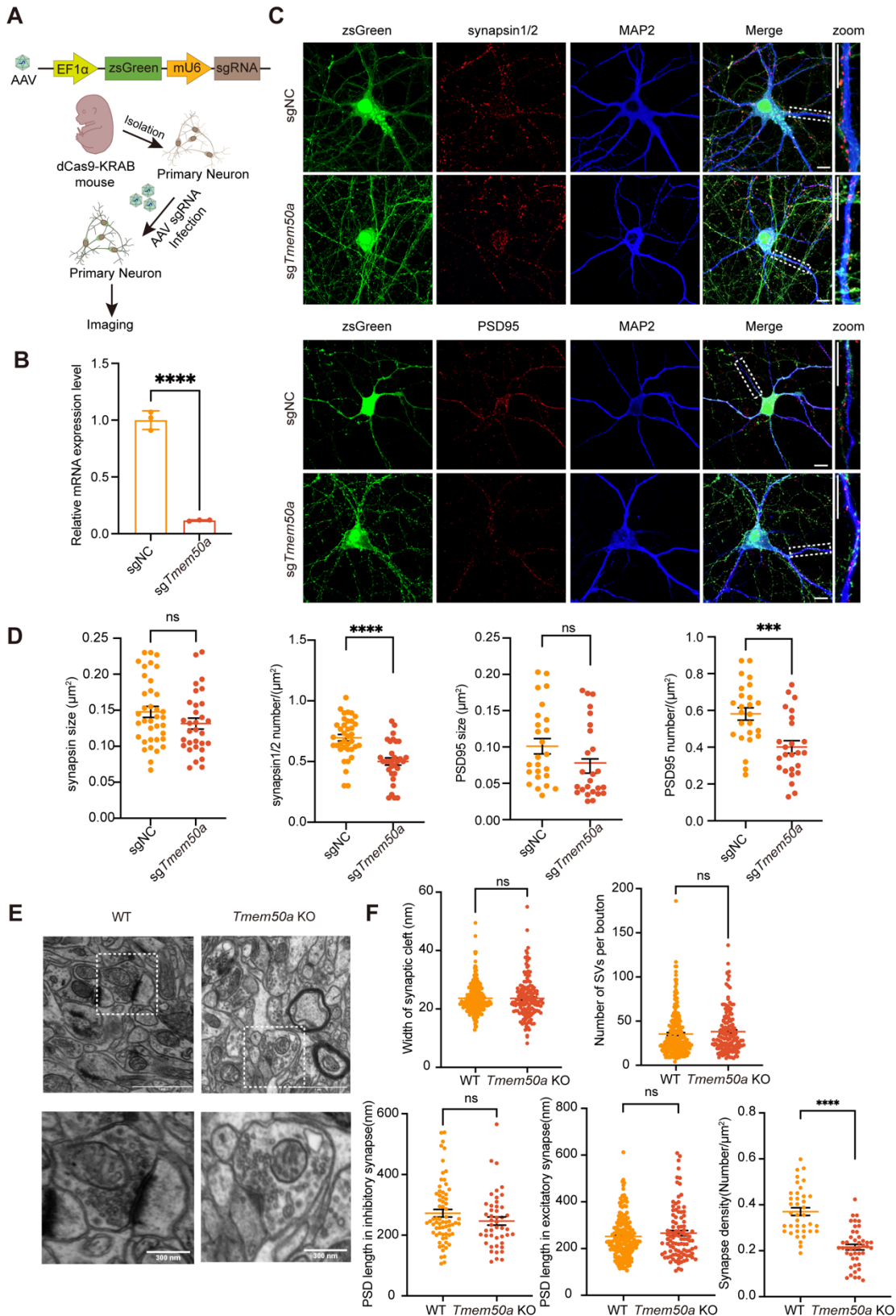
1238 (B) Volcano plot of plasma membrane proteins comparing *TMEM50A* KO versus WT
1239 iNeurons. Significantly altered surface proteins are highlighted in red.

1240 (C) Gene Ontology (GO) enrichment analysis (Biological Process) of significantly
1241 changed surface proteins in *TMEM50A* KO neurons. Top 10 significantly enriched
1242 terms are shown.

1243 (D) Representative confocal images of WT and *TMEM50A* KO iNeuron lines stained
1244 for MAP2 (dendrites, purple), synapsin1/2 (presynaptic marker, green), and PSD95
1245 (postsynaptic marker, red). Merged and zoomed views (right) show synaptic puncta
1246 along MAP2 dendrites. Scale bars, 10 μ m.

1247 (E) Quantification of synaptic puncta. Top: synapsin1/2 puncta size per neuron; second:
1248 synapsin1/2 puncta density per μ m dendrite length; third: PSD95 puncta size; bottom:
1249 PSD95 puncta density. Data are presented as mean \pm SEM (WT: n = 16; *TMEM50A*
1250 KO #1: n= 16; *TMEM50A* KO #2: n=10). ns, not significant, **p < 0.01, ***p < 0.001,
1251 one-way ANOVA.

1252



1253

1254 **Figure 6. *Tmem50a* loss decreases synapse density in primary neurons and *in vivo***

1255 (A) Schematic of CRISPRi-mediated knockdown of *Tmem50a* in primary cortical
1256 neurons. Primary neurons from dCas9-KRAB mice were infected with AAV expressing

1257 either a non-targeting control sgRNA (sgNC) or a *Tmem50a*-targeting sgRNA together
1258 with zsGreen for labeling.

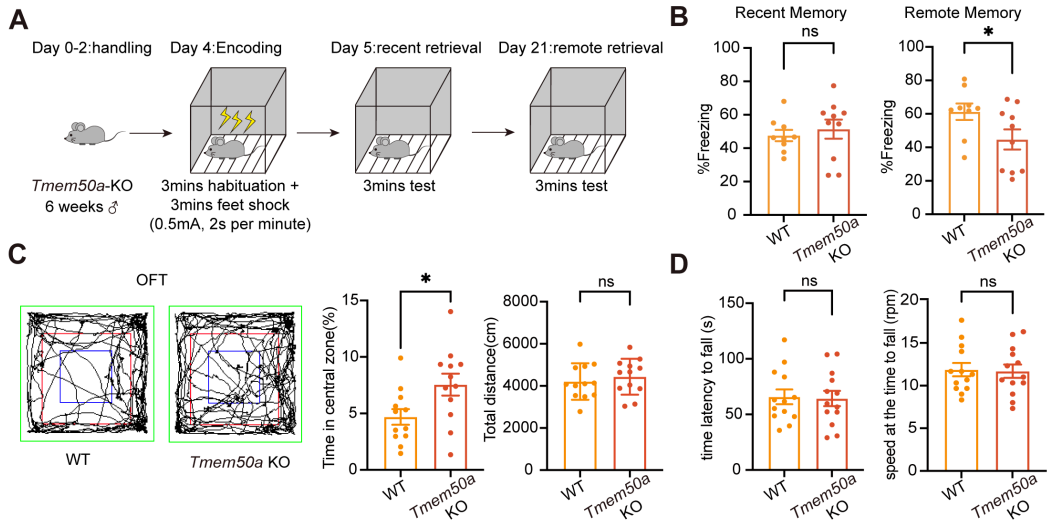
1259 (B) qRT-PCR validation of *Tmem50a* knockdown efficiency in primary neurons
1260 transduced with sg*Tmem50a* compared with sgNC. Data are presented as mean \pm SD
1261 (n = 3 biological replicates). ****P < 0.0001, unpaired t test.

1262 (C) Representative immunofluorescence images of sgNC and sg*Tmem50a* primary
1263 neurons stained for synapsin1/2 (up, red) or PSD95 (bottom, red) together with MAP2
1264 (blue), with zoomed-in views showing synaptic puncta. zsGreen, infection marker.
1265 Scale bars: 10 μ m.

1266 (D) Quantification of Synapsin1/2 and PSD95 puncta density and size in sgNC and
1267 sg*Tmem50a* neurons. Data are presented as mean \pm SEM (synapsin1/2 sgNC: n = 37,
1268 sg*Tmem50a*: n = 31; PSD95 sgNC: n = 25, sg*Tmem50a*: n = 25). ns, not significant,
1269 ***p < 0.001, ****p < 0.0001, unpaired t test.

1270 (E) Representative electron microscopy images of the ultrastructural of synapse in the
1271 ACC region of WT and *Tmem50a*-KO mouse brain tissue. Scale bars, as indicated.

1272 (F) Quantification of synaptic cleft width (WT n = 237, KO n = 146), synaptic vesicle
1273 (SV) number per bouton (WT n = 233, KO n = 151), PSD length at inhibitory (WT n =
1274 64, KO n = 48) and excitatory synapses (WT n = 175, KO n = 100), and synapse density
1275 (WT n = 38, KO n = 45) in the ACC region of WT and *Tmem50a*-KO mouse brain
1276 tissue. Data are presented as mean \pm SEM. ns, not significant, ***p < 0.0001, unpaired
1277 t-test.



1278

1279 **Figure 7. *Tmem50a* loss impairs remote memory and alters anxiety-like behavior**
1280 **without affecting motor coordination**

1281 (A) Schematic of the contextual fear conditioning paradigm.

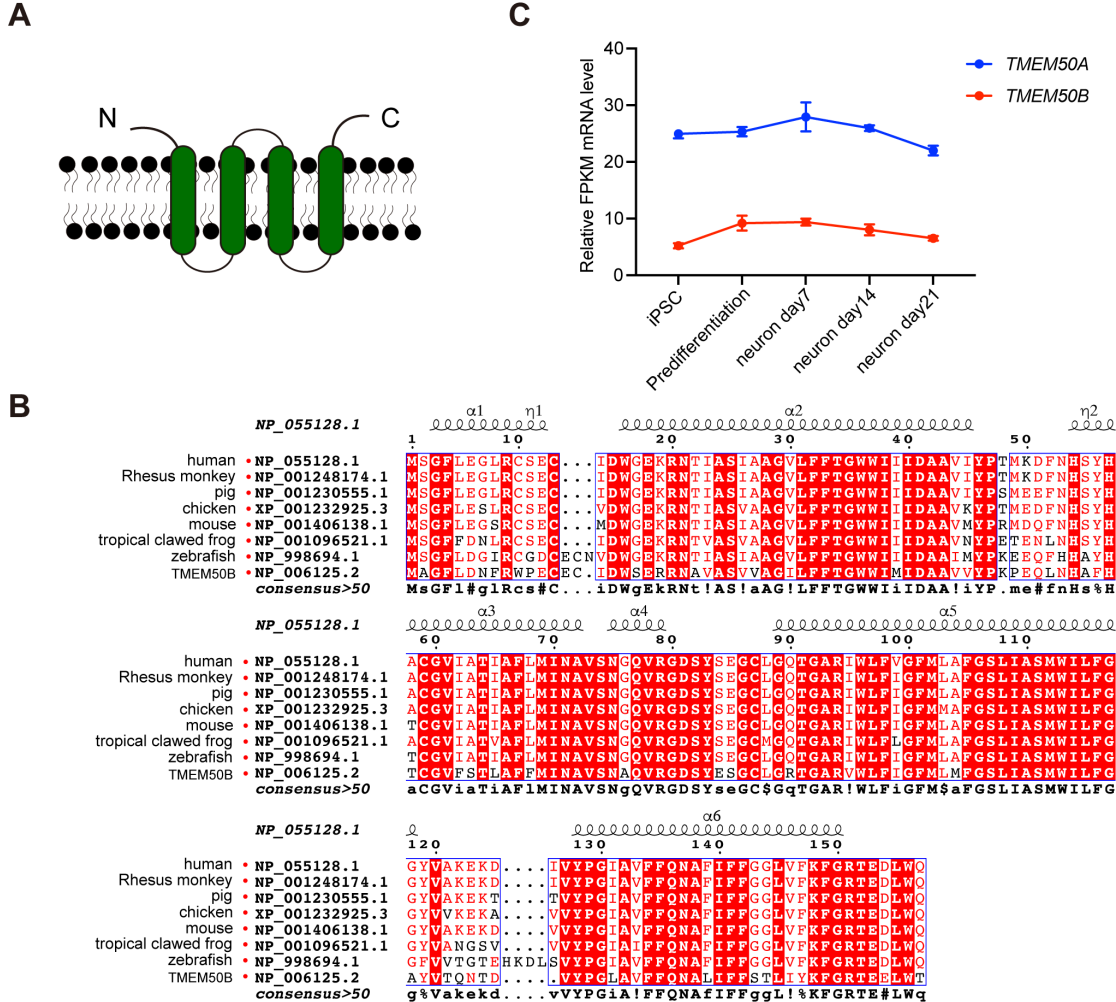
1282 (B) Freezing behavior during recent (Day 5) and remote (Day 21) memory retrieval.

1283 *Tmem50a*-KO mice show normal recent memory but significantly reduced freezing
1284 during remote memory retrieval compared with WT controls. Data are presented as
1285 mean \pm SEM (WT mice: n = 9, KO mice: n = 10). ns, not significant, *p < 0.05, unpaired
1286 t test.

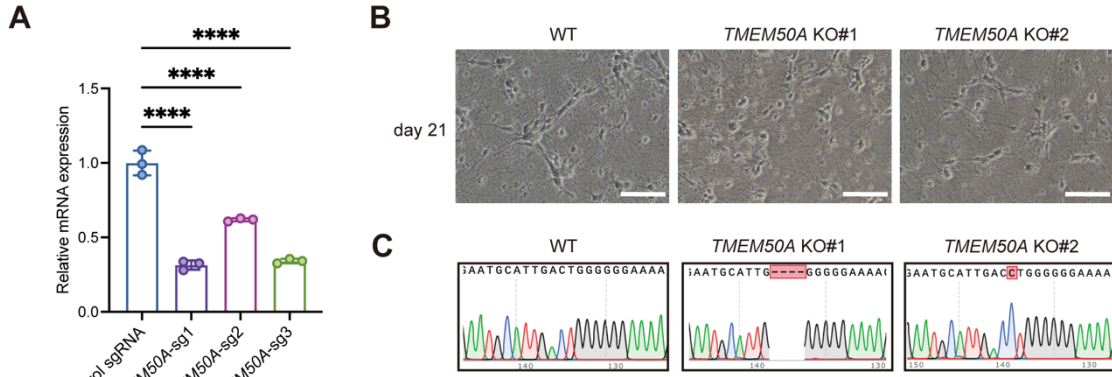
1287 (C) Open field test. Left: representative locomotor traces of WT and *Tmem50a*-KO
1288 mice (central zone outlined in green). Right: quantification of time spent in the central
1289 zone and total distance traveled. *Tmem50a*-KO mice spend more time in the center
1290 (reduced anxiety-like behavior) with no change in total distance. Data are presented as
1291 mean \pm SEM (n = 12). ns, not significant, *p < 0.05, unpaired t test.

1292 (D) Rotarod test. Latency to fall and speed at the time of fall are shown for WT and
1293 *Tmem50a*-KO mice. No significant differences were observed, indicating normal motor
1294 coordination and balance. Data are presented as mean \pm SEM (n = 13). ns, not significant,
1295 unpaired t test.

1296



1310 higher levels than *TMEM50B* at all stages. Data are presented as mean \pm SD (n = 3
1311 biological replicates).



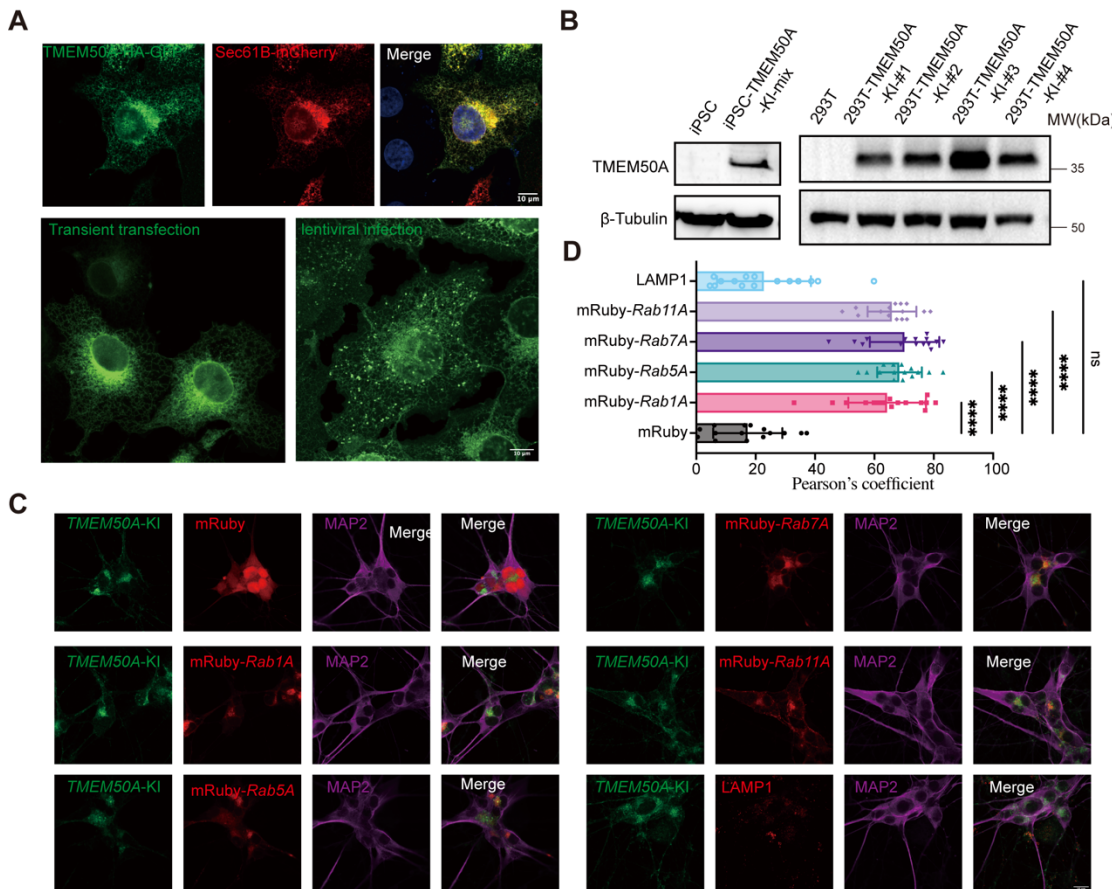
1312

1313 **Figure S2. Validation of *TMEM50A* knockdown and KO in iNeurons**

1314 (A) RT-qPCR analysis of *TMEM50A* expression in WT and *TMEM50A* knockdown
1315 iNeurons. Data are shown as mean \pm SD ($n = 3$). ***p < 0.0001, one-way ANOVA.
1316 (B). Representative phase-contrast images of WT and *TMEM50A* KO iNeurons at Day
1317 21, showing comparable overall neuronal morphology. Scale bars, as indicated.
1318 (C). Sanger sequencing of WT and *TMEM50A* KO iNeurons confirming the genetic
1319 knockout in two independent clones (KO#1 and KO#2).

1320

1321



1322

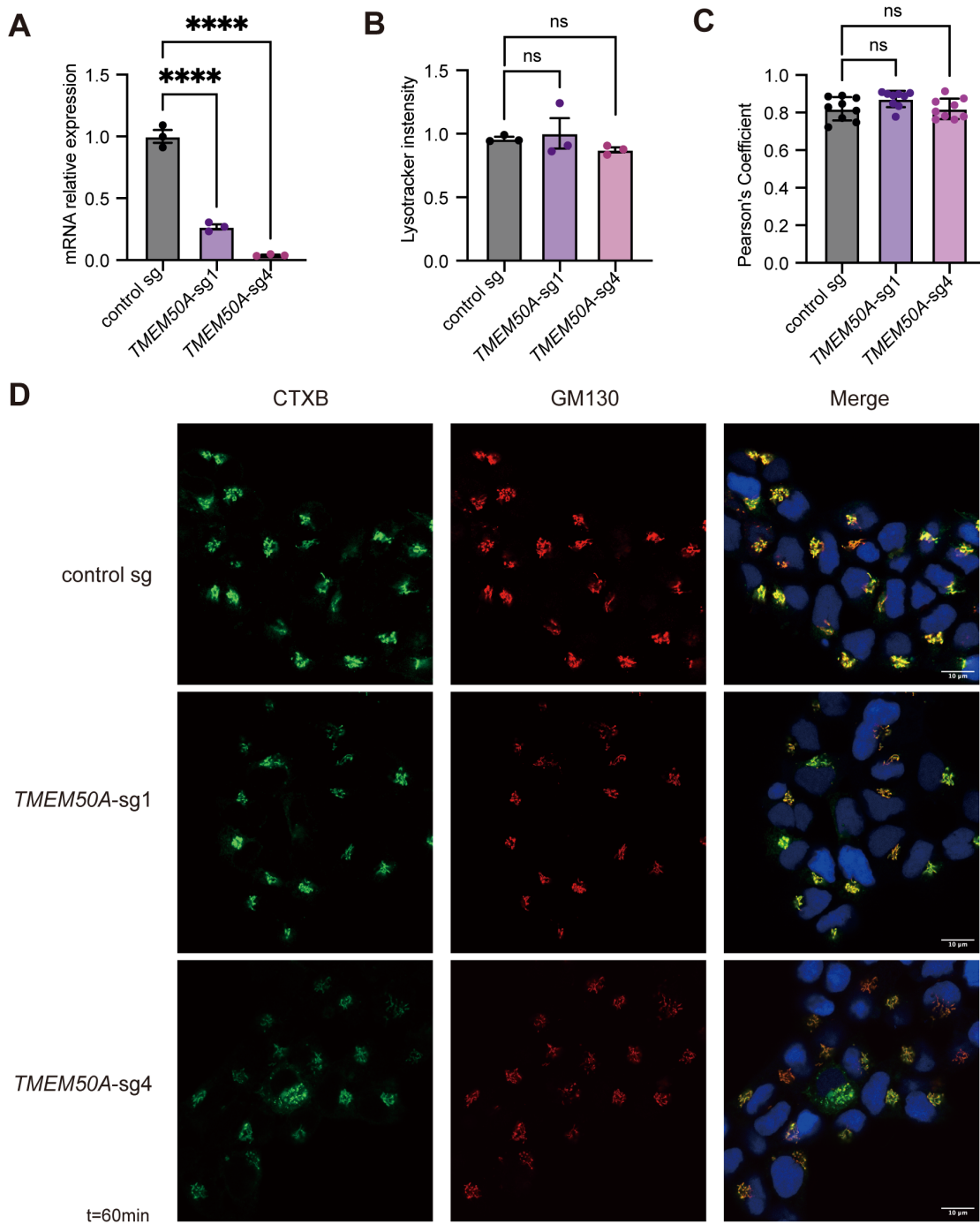
Figure S3. TMEM50A localizes to endosomal compartments but not lysosomes

1323 (A) Localization of exogenously expressed *TMEM50A* is affected by its overexpression
1324 levels. transient transfection produces prominent ER/reticular localization (top and
1325 bottom left), whereas lower-level lentiviral expression reveals predominantly
1326 punctate/vesicular *TMEM50A* distribution (bottom right). Scale bars, 10 μ m.

1327
1328 (B) Western blot validation of *TMEM50A*-3 \times FLAG-mNeonGreen KI in hiPSCs and
1329 HEK293T cells with anti-Flag antibody.

1330 (C) Representative immunofluorescence images of *TMEM50A*-KI iNeurons (green)
1331 with endosomal and lysosomal markers as indicated (red) and stained for MAP2
1332 (purple). Scale bar, 10 μ m.

1333 (D) Quantification of co-localization between *TMEM50A*-KI and indicated
1334 compartments using Pearson's correlation coefficient. Data are shown as mean
1335 \pm SD (n = 15 imaging fields). ns, not significant. ****p < 0.0001, one-way ANOVA.



1339 (A) qRT-PCR analysis confirming efficient *TMEM50A* knockdown in HEK293T cells
1340 expressing two independent *TMEM50A*-targeting sgRNAs (*TMEM50A-sg1*,
1341 *TMEM50A-sg4*) compared with control sgRNA. Data are presented as mean \pm SD (n =
1342 3 technical replicates). ****p < 0.0001, one-way ANOVA.

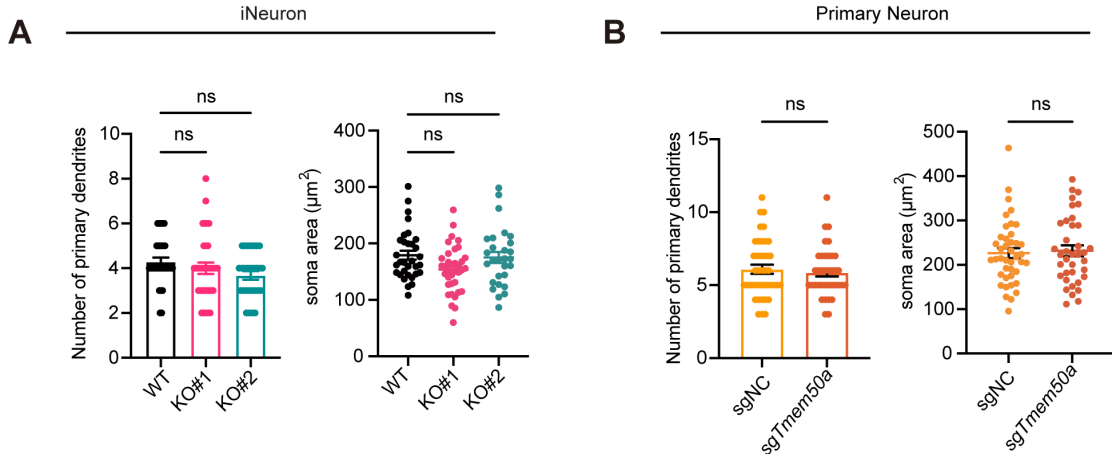
1343 (B) Quantification of Lysotracker fluorescence intensity in control and

1344 *TMEM50A*-knockdown HEK293T cells. Data are mean \pm SD (n = 3 technical
1345 replicates). ns, not significant, one-way ANOVA.

1346 (C) Quantification of the Pearson's correlation coefficient measuring colocalization of
1347 GM130 and CTxB. Data are mean \pm SD (n = 8 imaging fields). ns, not significant,
1348 one-way ANOVA.

1349 (D) Representative confocal images of CTxB (green) and GM130 (red) in control and
1350 *TMEM50A*-knockdown HEK293T cells after a 60-min chase, with nuclei stained by
1351 DAPI (blue). Scale bar, 10 μ m.

1352



1353

1354 **Figure S5. TMEM50A loss does not affect neuronal morphology**

1355 Quantifications of number of primary dendrites and soma area in iNeurons (A) (WT
1356 n=32, KO#1 n=36, KO#2 n=28, ns, not significant, one-way ANOVA) and primary
1357 mouse neurons (B) (sgNC n=41, sg *Tmem50a*=37, ns, not significant, unpaired t test).
1358 Data was analysed using same confocal images from Figure 5&6.

1359

1360 **Supplementary Materials**

1361 Table S1: sgRNA protospacer sequences for the memory-associated gene library

1362 Table S2: sgRNA counts and MAGeCK-iNC analysis results from the CaMPARI2-

1363 CRISPRi screen

1364 Table S3: sgRNA and primer sequences used in this study

1365 Table S4: TMEM50A interactome identified by IP-MS

1366 Table S5: Surface proteome comparing TMEM50A KO and WT iNeurons

1367